



1 **Extraordinary bloom of toxin-producing phytoplankton enhanced by**  
2 **strong retention in offshore continental shelf waters**

3

4 Valeria Ana Guinder\*<sup>1</sup>, Urban Tillmann<sup>2</sup>, Martin Rivarossa<sup>3</sup>, Carola Ferronato<sup>1</sup>, Fernando J. Ramírez<sup>1</sup>,  
5 Bernd Krock<sup>2</sup>, Haifeng Gu<sup>4</sup>, Martin Saraceno<sup>5,6,7</sup>

6

7 <sup>1</sup> Instituto Argentino de Oceanografía (IADO), Consejo Nacional de Investigaciones Científicas y Técnicas (CONICET),  
8 Argentina. Universidad Nacional del Sur, UNS. Florida 4750, 8000 Bahía Blanca, Argentina.

9 <sup>2</sup> Alfred Wegener Institut-Helmholtz Zentrum für Polar- und Meeresforschung, Am Handelshafen 12, 27570 Bremerhaven,  
10 Germany.

11 <sup>3</sup> Instituto Nacional de Investigación y Desarrollo Pesquero, INIDEP, and CONICET. Paseo Victoria Ocampo, Escollera Norte  
12 1, B7602HSA Mar del Plata, Argentina.

13 <sup>4</sup> Third Institute of Oceanography, Ministry of Natural Resources, Xiamen 361005, China.

14 <sup>5</sup> Centro de Investigaciones del Mar y de la Atmósfera (CIMA), CONICET, Facultad de Ciencias Exactas y Naturales,  
15 Universidad de Buenos Aires (UBA), C1063ACV, Buenos Aires, Argentina.

16 <sup>6</sup> Instituto Franco-Argentino de Estudio sobre el Clima y sus Impactos (IFAECI) CNRS-IRD-UBA-CONICET, Buenos Aires.

17 <sup>7</sup> Departamento de Ciencias del Océano y de la Atmósfera (DCAO), Facultad de Ciencias Exactas y Naturales, Universidad  
18 de Buenos Aires (UBA), C1063ACV, Buenos Aires, Argentina.

19

20 \*Correspondence to: [yguinder@iado-conicet.gob.ar](mailto:yguinder@iado-conicet.gob.ar)

21

22

23 **Abstract:**

24 The extensive Patagonian continental shelf in the Atlantic Ocean is renowned for its high productivity associated with nutrient-  
25 rich waters that fertilise massive phytoplankton blooms, especially along the shelf-break frontal system. Growing evidence  
26 reflects this ecosystem as a hotspot for harmful algal blooms (HABs). Whether these HABs reach coastal areas or are exported  
27 to the adjacent ocean basin by energetic edge currents remains unexplored. During two oceanographic cruises in spring 2021,  
28 a bloom of dinoflagellates of the Amphidomataceae family was sampled over the outer shelf with a ten-day interval, at stations  
29 40 km apart. The bloom was first sampled on November 16, with 32 million cells L<sup>-1</sup>, and was still persistent on November  
30 25, with 14 million cells L<sup>-1</sup>. The magnitude of this bloom is a global record for this group so far reported in the literature. The  
31 toxin azaspiracid-2 was detected in both stages of the bloom, with values up to 2122 pg L<sup>-1</sup>. The most likely source of AZA-2  
32 was *Azadinium spinosum* ribotype B. The bloom developed in vertically stable waters (60 m mixed layer depth) with elevated  
33 chlorophyll concentration. Water retention and the presence of fronts induced by horizontal stirring controlled the persistence  
34 and trajectory of the bloom in a localised area over the continental shelf, as evidenced by analysis of geostrophic surface  
35 currents, Lyapunov coefficients, and particle advection modelling. These findings underscore the importance of monitoring  
36 HABs in offshore environments, and the need to understand bio-physical interactions that govern bloom taxa assemblages and  
37 transport pathways.

38

39

40

41



## 42 1. Introduction

43

44 In marine environments, dinoflagellates are the primary toxin-producing group of protistan plankton and key causative agents  
45 of harmful algal blooms (HABs). As the most diverse group of toxic microorganisms, -e.g. *Alexandrium* spp., *Karenia* spp.,  
46 *Dinophysis* spp., *Azadinium* spp., *Amphidoma* spp.-, dinoflagellates produce a wide range of toxins. Phycotoxins are natural  
47 intracellular metabolites synthesised by certain microalgae that can be transferred through the food web, having severe impacts  
48 on marine biota, ecosystems and human health (Anderson et al., 2015; Sunesen et al., 2021). In the Argentine Sea, records of  
49 HABs caused by different plankton species have risen since the first documentation of human poisoning in spring 1980 caused  
50 by paralytic shellfish toxins (PST), produced by *Alexandrium catenella* in coastal areas (reviewed in Ramírez et al., 2022).  
51 Broadly, HABs were long thought to occur exclusively in coastal regions, due to their visible impacts on water quality and  
52 human-related activities, as documented for instance in the Argentine Patagonian Gulfs (Wilson et al., 2015; D'Agostino et  
53 al., 2019) and the Beagle Channel (Almandoz et al., 2019; Cadaillon et al., 2024). However, the perception of HABs as solely  
54 coastal events was biased, primarily due to greater monitoring efforts in coastal areas compared to the fewer studies conducted  
55 offshore (Hallegraeff et al., 2021; Sunesen et al., 2021; Anderson et al., 2021). In line with this trend, the expansion of the  
56 monitored area over recent decades have confirmed that toxic species are indeed common in offshore waters in the Argentine  
57 Sea (Ramírez et al., 2022), especially in the outer continental shelf associated to the shelf-break front (reviewed in Guinder et  
58 al., 2024). Furthermore, the increase in oceanographic studies focused on detecting HABs along the outer Patagonian shelf has  
59 led to several new records of toxin-producing species and phycotoxins in the South Atlantic (Akselman et al., 2015; Guinder  
60 et al., 2018; Tillmann et al., 2019). In particular, large HABs formed by the nano-dinoflagellates of the Amphidomataceae  
61 family —producers of the toxin azaspiracids— have emerged as important hazards in the productive Patagonian shelf-break  
62 frontal ecosystem (Guinder et al., 2024). It is well known that dinoflagellates possess advantageous strategies for thriving in  
63 frontal systems, such as effective swimming, mucus and cyst formation, mixotrophy, and toxin production (Smayda, 2002;  
64 Glibert, 2016). However, the bio-physical mechanisms explaining the development of large harmful blooms on  
65 hydrographically complex shelves are still not fully understood mainly due to the lack of simultaneous taxonomic data and  
66 velocity fields at synoptic scales.

67 The extensive Patagonian shelf-break front (35-55°S) in the SW Atlantic Ocean is a high productivity ecosystem, located ~200  
68 to ~900 km offshore (Martinetto et al., 2019; Guinder et al., 2024). This permanent termohaline front is associated with the  
69 upwelling of nutrient-rich waters of the westerly edge of the Malvinas Current, which fertilises the surface waters over the  
70 shelf (Palma et al., 2008; Matano et al., 2010). Additionally, over the mid shelf, the Patagonian Current transports diluted  
71 subantarctic waters northwards, also loading with nutrients the region. Hence, massive phytoplankton proliferations occur over  
72 the shelf in spring and summer (García et al., 2008; Carreto et al., 2016; Ferronato et al., 2023), including a variety of HAB-  
73 forming taxa and associated phycotoxins. The most conspicuous HABs are those formed by the dinoflagellates of the clade  
74 Amphidomataceae (Akselman and Negri, 2012; Fabro et al., 2019; Guinder et al., 2020; Tillmann et al., 2018; 2019), which  
75 include the four azaspiracids (AZAs)-producing species, i.e. *Azadinium dexteroporum*, *Az. poporum*, *Az. spinosum*, and  
76 *Amphidoma languida* (Krock et al. 2019). Amphidomataceans have been reported from different marine regions globally  
77 (Tillmann, 2018; Salas et al., 2021; Liu et al., 2023) but so far, the maximum bloom abundances reported in the literature are  
78 from the Argentine Sea (Akselman and Negri, 2012). During the springs of 1991 and 1992, these dinoflagellates reached  
79 between 3 and 9 million cells per litre and caused water discoloration in the northern area (38-42°S; 58°-56°W) of the  
80 Patagonian shelf (Akselman and Negri, 2012). No toxin screening was performed at that time, but in spring 2015, the  
81 production of AZAs was confirmed in another large bloom in the area (Tillmann et al., 2019). Moreover, AZAs have been  
82 detected in the tissue of the scallop *Zygochlamys patagonica* since the early 90ies (Turner and Goya, 2015). These scallops  
83 form large seabed banks along the 100-metre isobath between 38°S-48°S (Alemany et al., 2024), associated with the high  
84 phytoplankton productivity over the outer Patagonian continental shelf.



85 Despite the limited synoptic sampling in offshore waters, the prevalence of HABs in the Patagonian front highlights this  
86 ecosystem as a hotspot that requires further monitoring. The notably high abundance of Amphidomataceans over the outer  
87 shelf holds greater significance when assessing the potential risks posed to both regional and global ecosystems. The evolution  
88 and transport of HABs remain poorly understood, as does the question of whether they may reach coastal areas or be exported  
89 offshore into the stirring Atlantic Ocean. In this study, we characterised the bio-physical aspects of a large multispecific spring  
90 bloom of Amphidomataceans, detected through an unusual sampling effort that involved two research expeditions in  
91 November 2021. This HAB was observed at two sampling sites 40 km apart within a span of 10 days. In oceanic waters, the  
92 permanence and spatial extent of discrete phytoplankton blooms are influenced by dispersal mechanisms that rely on diffusion  
93 and horizontal advection (Abraham et al., 2000; Mahadevan, 2016; Lehahn et al., 2017). Typically, the dispersion and stirring  
94 of phytoplankton blooms in the ocean have been studied using remote sensing of chlorophyll-*a* and models (Lehahn et al.,  
95 2007; Lévy et al., 2018; Ser-Giacomi et al., 2023), with few studies considering *in situ* sampling (Abraham et al., 2000;  
96 Giddings et al., 2014; Hernández-Carrasco et al., 2020) to assess the bio-physical couplings of bloom development. Aside  
97 from the key role of mesoscale energetic variability in modulating phytoplankton community, observational studies combining  
98 multiple approaches at synoptic scale are still scarce. Here, we combined field observations of protistan plankton species  
99 composition and associated toxins, with remotely sensed ocean colour images of chlorophyll-*a* and geostrophic surface  
100 currents, particle tracking experiments, and Lyapunov coefficient analysis to assess the horizontal displacement and retention  
101 of the Amphidomataceae bloom within a mesoscale eddy. Furthermore, we aim to explore whether this HAB that developed  
102 in offshore shelf waters might reach coastal areas or be advected by the Malvinas Current, facilitating the dispersal of toxic  
103 species to other shelves and ocean basins.

104

## 105 2. Materials and Methods

106

### 107 2.1 Hydrography and productivity in the Patagonian continental shelf

108

109 Along the external margin of the Patagonian continental shelf, between 35°S and 55°S, a thermohaline front develops  
110 throughout the year, characterised by high biological productivity. The development of this front and the associated upwelling  
111 is due to the interaction of the energetic western boundary current system with the steep slope and the waters of the shelf, as  
112 well as the effect of winds and tides (reviewed in Piola et al., 2024). The Malvinas Current originates at ~55°S as a branch of  
113 the Antarctic Circumpolar Current (**Fig. 1**) and runs northwards at high velocity (mean surface velocities 45 cm/s, Piola et al.,  
114 2024) along the shelf break in two jets that meet at ~44°S (Frey et al., 2023). Then, at ~38°S, the Malvinas Current meets the  
115 warm and oligotrophic Brazil Current, which runs southwards, in the so-called Brazil-Malvinas Confluence, and waters are  
116 exported eastwards into the South Atlantic Ocean basin (**Fig. 1**). In addition, another branch of the Antarctic Circumpolar  
117 Current gives origin to the Patagonian Current which runs northwards over the continental shelf, carrying diluted subantarctic  
118 waters (**Fig. 1**).

119 The interaction of the Malvinas Current with the irregular bottom topography generates upwelling of cold, nutrient-rich waters  
120 that fertilise phytoplankton over the shelf, together with the Patagonian Current (reviewed in Guinder et al., 2024).  
121 Phytoplankton blooms expand over the mid and outer shelf as reflected by a persistent satellite chlorophyll-*a* band, wider in  
122 spring and narrower in summer along the shelf-beak front (Guinder et al., 2024). The magnitude of the upwelling has low  
123 seasonal variability and is heterogeneous along the extensive latitudinal range of the slope (Combes and Matano, 2018). Hence,  
124 productivity over the shelf varies spatially and temporally, and in consequence, multiple bioregions emerge, each characterised  
125 by unique phytoplankton phenological patterns, as revealed by climatological analysis of satellite-derived chlorophyll *a*  
126 (Delgado et al., 2023).

127

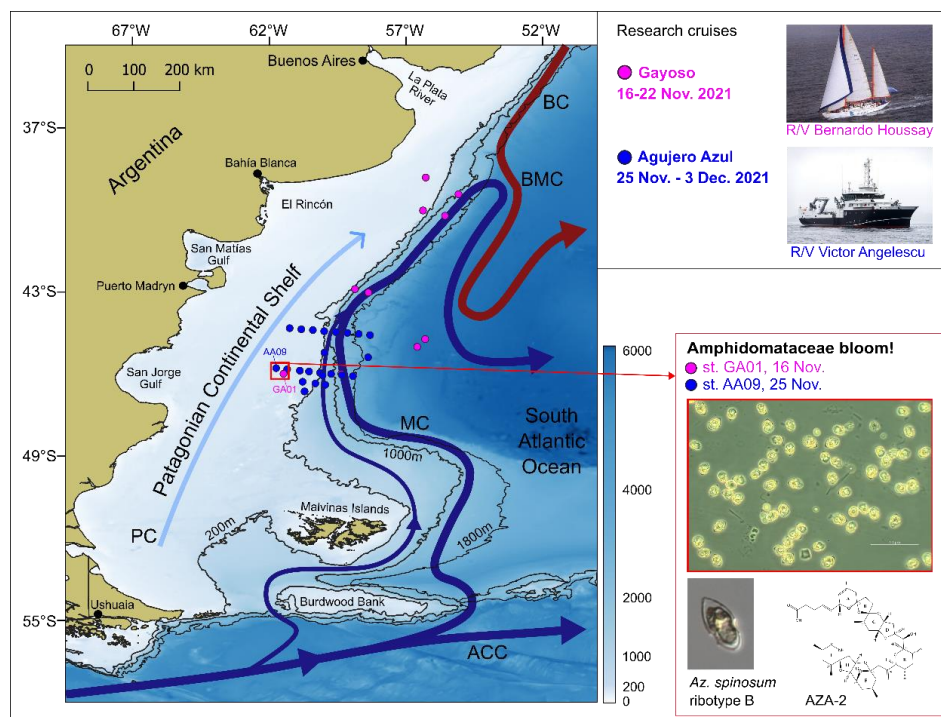


## 128 2.2 Research cruises

129

130 Two oceanographic expeditions were carried out during late-spring (November 2021) to study the microbial plankton  
131 communities in the Argentine continental shelf and adjacent ocean basin (**Fig. 1**). The first research cruise was the Ana María  
132 Gayoso (hereafter Gayoso, GA) onboard the R/V Bernardo Houssay (PNA and CONICET, Arg.), which covered a sampling  
133 period between 16 and 22 November 2021, at 10 stations along the outer Patagonian shelf, the core of the Malvinas Current,  
134 and adjacent open ocean waters (**Fig. 1**). The second cruise was the Agujero Azul (AA) onboard the R/V Victor Angelescu  
135 (INIDEP and CONICET, Arg.) which covered a sampling period between 25 November and 3 December 2021, at 23 stations  
136 aligned in two cross-shelf transects in the so-called Agujero Azul area (44-47°S; 62-57.5°W) (**Fig. 1**). We first provide a  
137 general overview of the sampling conducted in both cruises, but then we focus on the Amphidomataceae bloom observed over  
138 the shelf at station GA01 on 16 November and at station AA09 on 25 November, separated by *ca.* 40 km (**Fig. 1**).

139



140

141 **Figure 1:** Sampling stations of the research cruises Gayoso (pink dots, onboard R/V Houssay) and Agujero Azul (blue  
142 dots, onboard R/V Angelescu), and the main circulation pattern in the Argentine continental shelf and shelf break. The  
143 stations where the bloom of Amphidomataceae was observed are indicated with a red square: GA01 and AA09, sampled  
144 on November 16 and 25, respectively. Micrographs show the Amphidomatacean bloom and a cell of *Azadinium*  
145 *spinosum* ribotype B, producer of azaspiracid-2 (AZA-2). ACC: Antarctic Circumpolar Current, MC: Malvinas  
146 Current, BC: Brazil Current, BMC: Brazil-Malvinas Confluence and PC: Patagonian Current. Bathymetry from  
147 GEBCO, 2021. Isobaths of 200 m, 1000 m and 1800 m are displayed.

148

## 149 2.3 Remote sensing of surface Chl-*a*, SST and ADT

150

151 In order to contextualise the discrete observations of plankton within broader spatio-temporal dynamics, we explored satellite-  
152 derived surface chlorophyll-*a* concentration (Chl-*a* sat) data from the days of the cruises. In this sense, daily merged product



153 with a 4 km resolution, provided by the GlobColour project (distributed by ACRI ST, France: <https://hermes.acri.fr/>), were  
154 downloaded. This ocean color product is generated from the fusion of the SeaWiFS, MERIS, MODIS-Aqua, and OLCI sensors  
155 and estimates the average Chl-*a* concentration in the surface layer (Maritorena et al., 2010). The fusion of data from different  
156 satellite sensors, combined with the quality control criteria used by GlobColour, enables enhanced spatial and temporal  
157 coverage. Eight-day temporal averages were calculated for the periods of November 12–19 and November 20–27, 2021.  
158 Additionally, daily Chl-*a* images were assessed from November 14 to 27 focused on the bloom area to track its short-term  
159 evolution. Due to high cloud covering, data is missing from 22 to 24 November. To analyse Sea Surface Temperature (SST)  
160 during the sampling periods, daily NSST MODIS-Aqua level L3 images with a 4 km resolution were downloaded from  
161 <https://oceancolor.gsfc.nasa.gov/>. Eight-day temporal averages were also constructed for the periods of November 12–19 and  
162 November 20–27, 2021. All images were processed using SeaDAS v8.3 and QGIS 3.38, mapped to the WGS84 reference  
163 system (datum WGS84, ellipsoid WGS84), and restricted to the study area. The images were smoothed using a 'Non-Linear  
164 Mean 3x3' filter.

165 To compute trajectories of virtual particles (see Sect. 2.6 below) and Finite Size Lyapunov Exponents (FSLE, Sect. 2.7) we  
166 used Absolute Dynamic Topography (ADT) maps and geostrophic velocities derived from the ADT maps. Gridded ADT maps  
167 of daily temporal resolution and ¼ of degree spatial resolution maps were obtained from CMEMS  
168 (<https://marine.copernicus.eu/>). FSLE images with a spatial resolution of 1/25° grid were downloaded from AVISO  
169 (<https://www.aviso.altimetry.fr>).

170

#### 171 **2.4 *In situ* measurements and sample collection**

172

173 At each sampling station, continuous vertical profiles of temperature, salinity and fluorescence were measured. In Gayoso  
174 cruise, a Sea-Bird 9 plus CTD and a fluorometer sensor Wet Labs FLRTD-5105 were used. In Agujero Azul cruise, a Seabird  
175 SBE 9 Digiquartz CTD coupled with an ancillary Seapoint SCF chlorophyll fluorometer were used. To assess the vertical  
176 stability of the water column, the Brunt-Väisälä buoyancy frequency ( $\text{cyc h}^{-1}$ ) was computed using the function `swN2` of the  
177 package `oce` (Kelley et al. 2022) in R statistical software. Thereafter, the mixed layer depth (MLD, in metres) was defined at  
178 the depth where the maximum value of the Brunt-Väisälä frequency was detected.

179 Niskin bottles attached to the CTD-rosette were used to collect water samples at the surface (5 m depth) for the analysis of  
180 chlorophyll *a*, dissolved inorganic macronutrients, protistan plankton by microscopy, genetic analysis of the species diversity,  
181 and phycotoxins in field samples.

182 For chlorophyll *a*, a volume of 400 mL was filtered through filter GF/F fiber-glass filters pre-combusted at 450 °C for 4 h. A  
183 volume of 10 mL of 90 % acetone was used for pigment extraction during 24 hs (4 °C), and thereafter quantified using an  
184 Agilent Cary 60 UV-Vis spectrophotometer. Concentration was estimated using the equations developed by Jeffrey and  
185 Humphrey (1975).

186 For inorganic nutrients, the water samples filtered through Whatman GF/F fiber-glass filters pre-combusted at 450 °C for 4 h,  
187 were stored at -20 °C in alkali-rinsed (NaOH, 0.1 M) polyethylene bottles. Nitrite, nitrate, ammonium, silicate and phosphate  
188 were measured using a spectrophotometer Agilent Cary 60 UV-Vis following the method outlined by Hansen and Koroleff  
189 (1999).

190 Duplicate samples for plankton counts collected with Niskin bottles were preserved with Lugol (1% *f/c*) and formaldehyde  
191 (1% *f/c*) in glass bottles (250 mL) and kept in dark and at 4 °C for their analyses under microscopy. Similarly, duplicate water  
192 samples were collected by three vertical net tows (20 µm size pore) integrating the first 30 m depth for the identification of  
193 protists' taxa.

194 For the quantification of azaspiracids (AZAs) as well as for genetic analysis of field species diversity, the same sampling  
195 protocol was applied. A volume of 4-5 L of seawater from the Niskin bottles was pre-screened through a 20 µm mesh-size,



196 and subsequently filtered through 5  $\mu\text{m}$  pore-size polycarbonate filters (Millipore, Eschborn, Germany) under gentle vacuum  
197 ( $< 200$  mbar). Filters were placed in 50 mL centrifuge tubes and preserved at  $-80$  °C for further analyses in the laboratory.

198

## 199 **2.5 Microscopy analysis of protistan plankton**

200

201 Morphological aspects of plankton cells were carefully observed under different light microscopes all equipped with  
202 epifluorescence and differential interference contrast optics: a Nikon Eclipse E-400 microscope, a Zeiss Axioskop 2  
203 microscope, and an inverted Axiovert 200 M. In order to measure length and width of cells, micrographs were taken at 1000  
204 magnification under a Zeiss Axio Vert.A1 equipped with a digital camera AxioCam 208 Color, and under an Axioskop 2  
205 equipped with a Axiovision digital camera. Thereafter, they were processed with the software ZEN (v.2.7, Zeiss) and  
206 Axiovision (v.4.8, Zeiss). Further, scanning electron microscopy (SEM, FEI Quanta FEG 200) was used to assess detailed  
207 taxonomic features of the dinoflagellate species (e.g. arrangement of thecal plates, presence of pores and spines, etc). SEM  
208 samples were treated following the protocol described in Tillmann et al. (2017). For the estimation of total protists' abundance  
209 (in cells  $\text{L}^{-1}$ ), seawater samples collected with Niskin bottles and fixed with Lugol were settled in sedimentation chambers and  
210 single cells were counted under inverted microscope using a magnification of 400 following traditional techniques (Hasle,  
211 1987). All protists larger than 5  $\mu\text{m}$  in cell size were counted and classified into species or genera taxonomic levels, or merged  
212 into taxonomic/functional groups organized in size ranges (e.g. ciliates between 10-20  $\mu\text{m}$ , cryptophytes  $<10$   $\mu\text{m}$ ,  
213 *Gymnodinium*-type cell, Kareniaceae-type cell, etc.). In addition, to assess the relative abundance of the Amphidomataceae  
214 species responsible for the multispecific bloom of this clade, subsamples (10-mL) were carefully counted with high taxa  
215 resolution.

216

## 217 **2.6. Genetic analysis**

218

219 For a broad detection of amphidomatacean species diversity in field samples, metarbarcoding was performed specifically  
220 targeting the internal transcribed spacer (ITS1) region, following Liu et al. (2023). This information was used as a complement  
221 to the exhaustive morphological taxonomy performed under light microscopy and SEM, especially for the accurate  
222 identification of ribotypes.

223

## 224 **2.7 Toxin identification and quantification**

225

226 Filters were repeatedly rinsed with 500  $\mu\text{L}$  methanol until complete discoloration of the filters. The methanolic extracts were  
227 transferred to a spin-filter (0.45  $\mu\text{m}$  pore-size, Millipore) and centrifuged at  $800 \times g$  for 30 s, followed by transfer to  
228 autosampler vials and stored at  $-20$  °C until analysis. Toxin analyses were performed using high performance liquid  
229 chromatography coupled to tandem mass spectrometry HPLC-MS/MS in the selected reaction monitoring (SRM) mode for  
230 the detection of known AZA variants. In addition, precursor experiments of the ions  $m/z$  348, 350, 360, 362, and 378 were  
231 carried out to find potentially new AZA variants. Screened mass transitions and instrument parameters are detailed in Tillmann  
232 et al. (2021).

233

## 234 **2.6 Lagrangian analysis**

235

236 We used the geostrophic currents computed from satellite altimeter data (see Sect. 2.3) and an algorithm that represents the  
237 advection process caused by those currents to represent the trajectories of virtual neutrally buoyant particles. Particles were  
238 released at the surface along  $46^\circ\text{S}$  every 0.05 grades and in the four regions indicated in the **Appendix D**. The algorithm used





239 for the advection process is fully described in Haller and Beron-Vera (2012). The algorithm computes the particle positions  
240 based on initial location and knowledge of the velocity field. Therefore, the accuracy of the trajectories obtained relies on the  
241 accuracy of the geostrophic velocity field obtained from satellite altimetry. In the northern portion of the Argentine continental  
242 shelf, such surface velocities showed to be well correlated with in situ current measurements (Lago et al., 2021). We therefore  
243 assume that the surface dynamics can be represented by satellite altimetry derived data and use it as the input velocity field for  
244 the algorithm to advect the virtual particles.

245

## 246 **2.7 Lyapunov coefficient analysis**

247

248 In order to examine meso- and submesoscale frontal structures during phytoplankton blooms, daily finite-size Lyapunov  
249 exponent (FSLE) images from November 10 to 25 were analysed. Additionally, the daily images were used to create a video  
250 with Filmora v.11 (available in the **Appendix D**) to illustrate the daily evolution of the FSLE in the area where the  
251 phytoplankton bloom developed. The FSLE is obtained by measuring the backward-in-time divergence of initially nearby  
252 particles and it is commonly used as an indicator of frontal activity and stirring intensity. Relatively large FSLE values are  
253 associated with formerly distant water masses, whose confluence creates a transport front (d'Ovidio et al., 2004; d'Ovidio et  
254 al., 2009). Fronts identified as maxima (ridges) of FSLEs have a convergent dynamics transverse to them, so that passive  
255 particles in their neighbourhood are attracted to the front and then advected along it (Della Penna et al., 2015).

256

## 257 **3. Results**

258

### 259 **3.1 Satellite-derived chlorophyll *a* during the sampling period**

260

261 During the Gayoso cruise (12-19 Nov, **Fig. 2a**), a uniform, large band of high surface Chl-*a* concentration expanded over the  
262 mid and outer shelf. During the Agujero Azul cruise (20-27 Nov, **Fig. 2b**), the band of Chl-*a* disaggregated and showed lower  
263 intensity, but the Chl-*a* concentration was still high in the area of the sampling stations (**Fig. 2b**). The distribution of Chl-*a*  
264 concentration during the time of the cruises is indicative of mid-late spring phytoplankton bloom (November) over the  
265 Patagonian shelf which typically exhibits higher concentration south of 43°S following the thermal stratification (**Fig. 2a, b**).  
266 The SST showed warming of the inner-mid shelf waters north of 44°S over the 8-day average periods (**Fig. 2c, d**), but the SST  
267 remained yet constant at the sampling stations' area (see **Fig. 4** and **Table 1**). The daily images of Chl-*a* from 14 to 25  
268 November (**Fig. 3**) showed an abrupt proliferation of phytoplankton on November 15 which notably intensified on November  
269 16 when it reached the maximum concentrations during the studied period. On this date, the extraordinary bloom of  
270 Amphidomataceae was sampled at GA01. During the following days, the chlorophyll levels remained high in the area but  
271 became more disaggregated into variable patches. On November 25, the sampling day at station AA09, Chl-*a* had decreased  
272 at station GA01 but remained intense at AA09 with still extraordinary densities of Amphidomataceans.

273

274

275

276

277

278

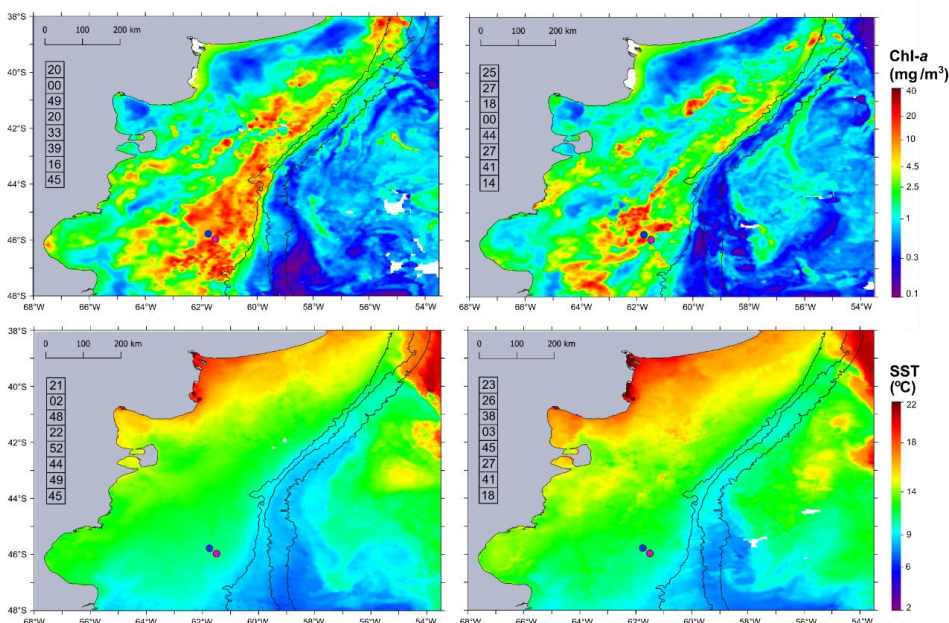
279

280

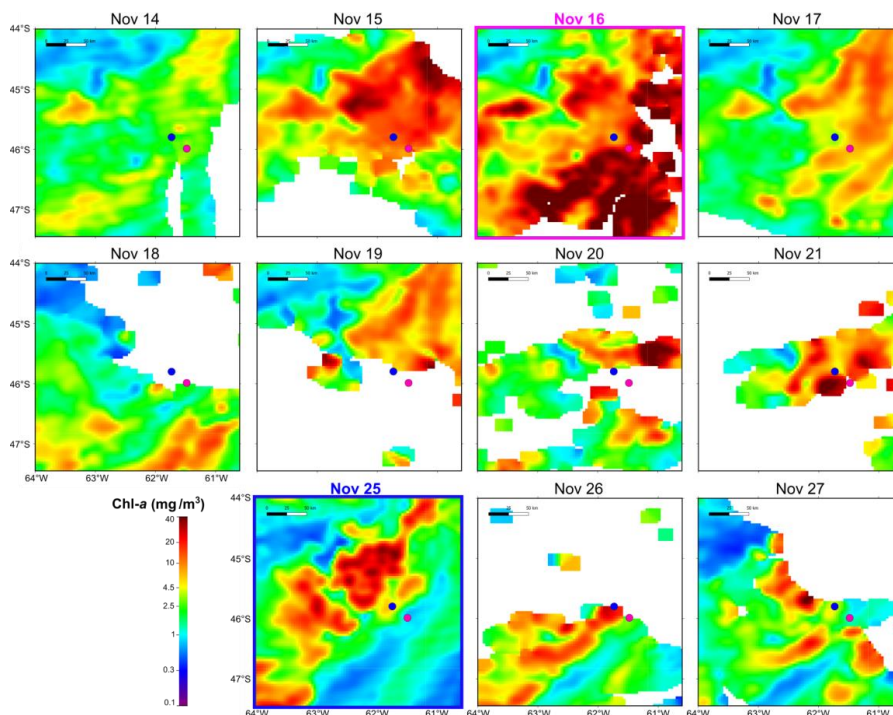
281



282  
283  
284  
285  
286  
287  
288  
289  
290  
291  
292  
293  
294  
295  
296  
297  
298



299 **Figure 2:** Eight-day time mean of (a, b) satellite chlorophyll *a* (Chl-*a* in mg/m<sup>3</sup>) and (c, d) sea surface temperature (SST  
300 in °C) during the sampling period: (a and c) 12-19 November 2021, and (b and d) 20-27 November 2021. From left to  
301 right, isobaths of 200, 1000 m and 1800 m are shown. The numbers in the column on the left side of each panel  
302 correspond to the percentage of cloud-free pixels in each daily satellite image. The sampling stations GA01 (pink dot)  
303 and AA09 (blue dot) are shown.



304  
305  
306

**Figure 3:** Daily satellite-derived surface chlorophyll-*a* in the area of the sampling stations: GA01 (pink dot, sampled on  
November 16, 2021), and AA09 (blue dot, sampled on November 25, 2021).

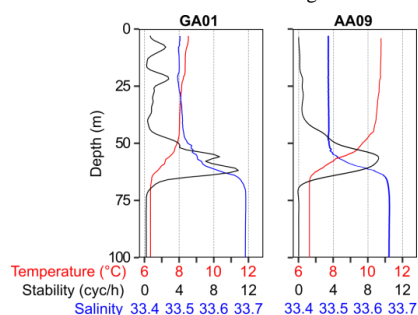




307 **3.2 *In situ* biogeochemical properties and water column structure**

308

309 A reddish water discoloration was observed in the bloom area (45.5–46°S, 62–61°W) during the cruises. Surface water  
 310 temperature and salinity remained similar at both stations GA01 and AA09 sampled with a ten-day interval (**Fig. 4, Table 1**).  
 311 Moreover, both stations displayed the same vertical structure in terms of temperature and salinity (**Fig. 4**), the mixed layer  
 312 depth (MLD), and the subsurface chlorophyll maximum (SCM) (**Table 1**). *In situ* chlorophyll-*a* concentration at the surface  
 313 was 20 µg L<sup>-1</sup> at GA01 and 4.5 µg L<sup>-1</sup> at AA09 (**Table 1**). Dissolved inorganic macronutrients in surface waters were similar  
 314 in both stages of the bloom, except for nitrate and silicate, which were higher at AA09. In particular, the silicate recovered by  
 315 ~5 times towards the advanced stage of the bloom.



316

317 **Figure 4: Vertical profiles of temperature, salinity, and stability measured at the two blooming stations, GA01 (sampled**  
 318 **on 16 Nov) and AA09 (sampled on 25 Nov). Strong stratification is denoted by the water column stability (Brunt-Väisälä**  
 319 **buoyancy frequency) which indicates a mix layer depth (MLD) around 60 m.**

320

321 **Table 1: Surface values of physical and chemical variables measured at stations GA01 and AA09. Sea surface**  
 322 **temperature (SST), sea surface salinity (SSS), and concentration of *in situ* chlorophyll-*a* (Chl-*a*), and macronutrients.**  
 323 **The depth of the subsurface chlorophyll maxima (SCM) and the mix layer depth (MLD) is also displayed.**

	GA01	AA09
Date	16-Nov	25-Nov
SST (°C)	10.5	10.9
SSS	33.5	33.5
SCM (m)	15	10-25
MLD (m)	60	55
Chl- <i>a</i> (µg L <sup>-1</sup> )	20.0	4.5
Nitrite (µM)	0.48	0.33
Nitrate (µM)	1.77	3.57
Ammonium (µM)	1.32	1.32
Silicate (µM)	4.54	22.35
Phosphate (µM)	0.33	0.44

324

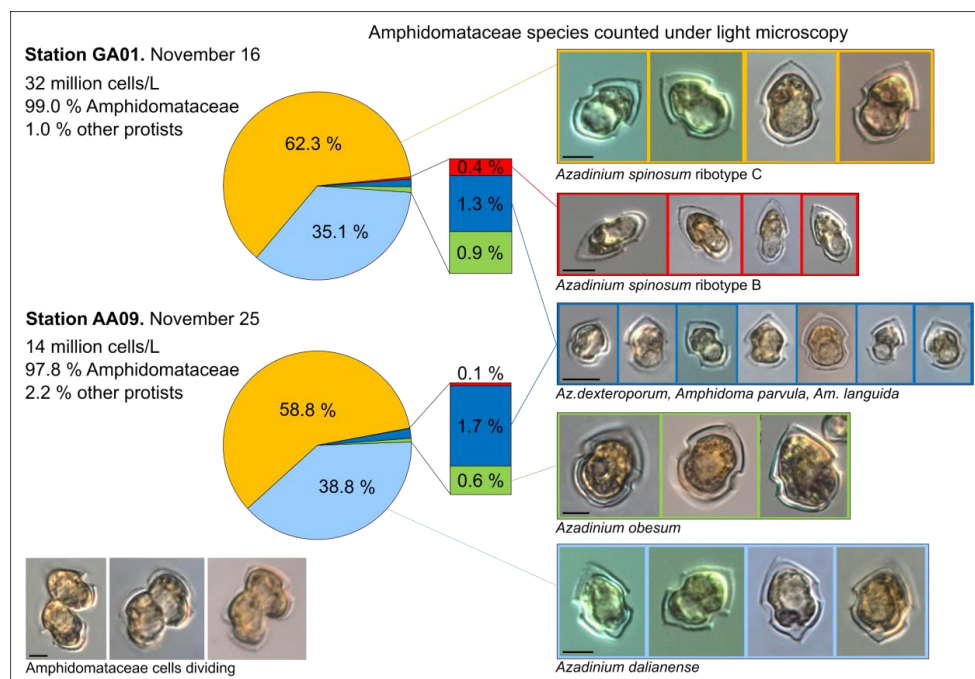
325 **3.3 Multispecificity of the Amphidomatacean bloom and azaspiracids**

326

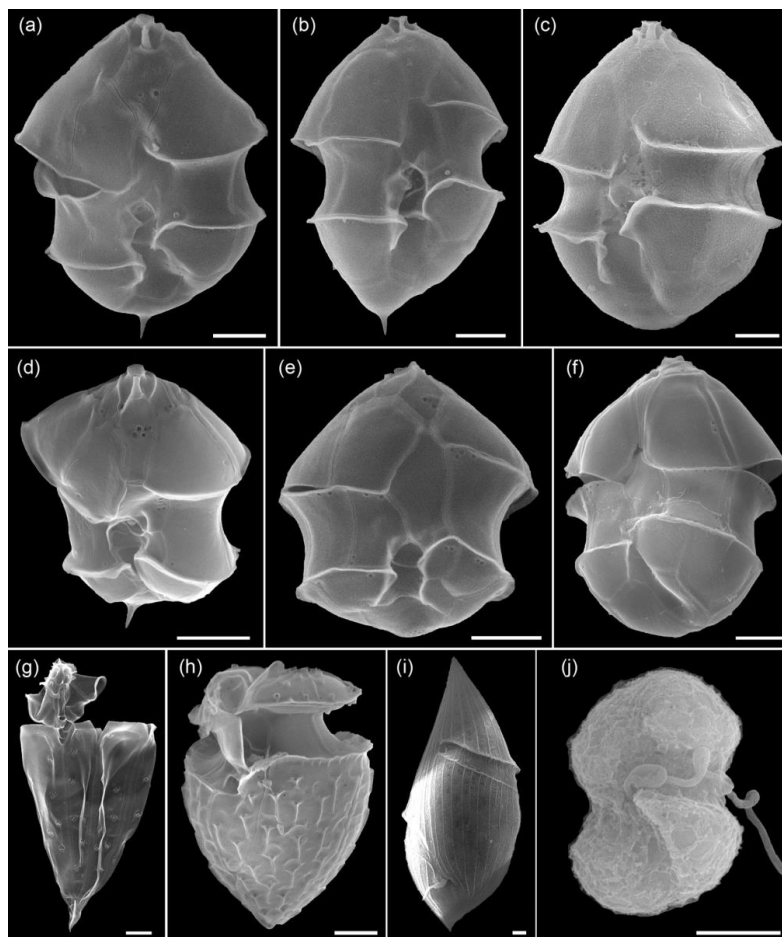
327 Total protistan plankton of cell size larger than 5µm reached up 31.68 x10<sup>6</sup> cells L<sup>-1</sup> at station GA01, and 10-days later at  
 328 station AA09, the abundance was 13.69 x10<sup>6</sup> cells L<sup>-1</sup>. Of all this total protist abundance, the Amphidomataceae clade  
 329 represented up to 99 % and 98 %, respectively (**Fig. 5**), mostly dominated by the non-toxicogenic species *Azadinium spinosum*  
 330 ribotype C and *Azadinium dalianense* (**Fig. 5 and 6**), representing together >95 % of total Amphidomataceae (**Fig. 5**).  
 331 Taxonomic identification up to species level was possible after exhaustive morphological examination of cells under light



332 microscopy (Fig. 5) and scanning electron microscopy (Fig. 6). In the Appendix A, more micrographs of Amphidomataceans  
 333 are shown taken under light microscopy and scanning electron microscopy (Figs. A01 to A10), along with the rationale for  
 334 the Amphidomatacean species designations. The ITS-based metabarcoding of species diversity detected in the field samples  
 335 at GA01 and AA09 are also shown in the Appendix B, which also support the dominance of *Azadinium spinosum* ribotype C  
 336 and *Azadinium dalianense*. In the detailed counting of protistan species in 10-mL subsamples, the well-recognized  
 337 Amphidomataceae species under inverted light microscopy for their individual quantification were: *Azadinium spinosum*  
 338 ribotype B and ribotype C, *Az. dalianense*, *Az. obesum*, and the smaller taxa *Az. dexteroporum*, *Amphidoma parvula* and *Am.*  
 339 *languida* (Fig. 5). This distinction was based on morphological aspects combining the cell size and shape, such as the  
 340 length/wide relation, and other taxonomic aspects. For instance, a slender shape: *Az. spinosum* ribotype B; round: *Az. obesum*,  
 341 short, tiny: *Az. dexteroporum*, *Amphidoma parvula* and *Am. languida*; with a bump in the hypotheca and a pyrenoid in the  
 342 hyposome: *Az. dalianense*; with a spine in the hypotheca: *Azadinium spinosum* ribotype C, *Az. dalianense*, and *Az.*  
 343 *dexteroporum*. These and other taxonomic features were further examined by SEM (Fig. 6), for example the number and  
 344 arrangement of the thecal plates, the presence of thecal pores, etc. (see the Appendix A). Finally, other protists than  
 345 Amphidomataceans (Fig. 7) contributed up to 1.0 and 2.2 % of the total abundance at stations GA01 and AA09, respectively.  
 346 Most of the other protists were heterotrophic and mixotrophic dinoflagellates and ciliates. No diatoms were observed in the  
 347 field samples. For an overview of the pure Amphidomataceae bloom in the field samples (e.g. no mucus formation, no  
 348 aggregates, cells undergoing cell division), low-magnification micrographs obtained through light microscopy are presented  
 349 in the Appendix C. The screen of all known and potentially novel variants of azaspiracids, which are produced by  
 350 Amphidomataceae, revealed the presence of solely azaspiracid-2 (AZA-2) in both stages of the bloom, with field values of  
 351 2122 pg L<sup>-1</sup> at GA01 and 620 pg L<sup>-1</sup> at AA09.  
 352



353  
 354 **Figure 5: Relative abundance (in %) of the Amphidomataceae species identified under light microscopy at stations**  
 355 **GA01 and AA09. The total abundance of protists at each station was 32 million cells L<sup>-1</sup> and 14 million cells L<sup>-1</sup>,**  
 356 **respectively. From the total cells counted, Amphidomataceae represented up to the 99.0 % and 97.8 %, respectively.**  
 357 **The colours in the pie charts correspond to the same species at both stations. Scale bar: 5 µm.**



358

359 **Figure 6:** Scanning electron microscopy of Amphidomataeae species (a-f) and other dinoflagellates (g-j) at stations  
360 GA01 and AA09. (a) *Azadinium spinosum*, (b) *Az. dalianense*, (c) *Az. obesum*, (d) *Az. dexteroporum*, (e) *Amphidoma*  
361 *parvula*, (f) *Am. languida*, (g) *Oxytoxum gracile*, (h) *Oxytoxum laticeps*, (i) *Gyrodinium* sp., (j) unidentified gymnodinoid  
362 species. Scale bars = 2  $\mu\text{m}$ . See the Appendix A for more micrographs of Amphidomataceans and for evidence and  
363 rationale for the Amphidomatacean species designations.

364

365



366

367 **Figure 7: Micrographs of other protists (1.0 - 2.2 % of total abundance) present in the bloom. a) *Oxytoxum laticeps*, b)**  
368 ***Gyrodinium spiralis*, c) *O. gracile*, d) *Karenia* sp., e) unidentified dinoflagellate, f) *Gyrodinium* sp., g-i) unidentified**  
369 **gymnodinoid cells, k-l) naked ciliates, m) *Peridiniella* sp., n) Karenia-type cell, o) Euglenophyte, p) *Lessardia***  
370 ***elongata*, q) *Torodinium robustum*, r) ciliate with an Amphidomataeae cell (arrow), s) ciliate, t) *Dinophysis* sp. Scale**  
371 **bar: 10  $\mu$ m, except in photos g) and h), scale bar 5  $\mu$ m.**

372

### 373 3.4 Surface currents, particle advection model and Lyapunov frontal systems

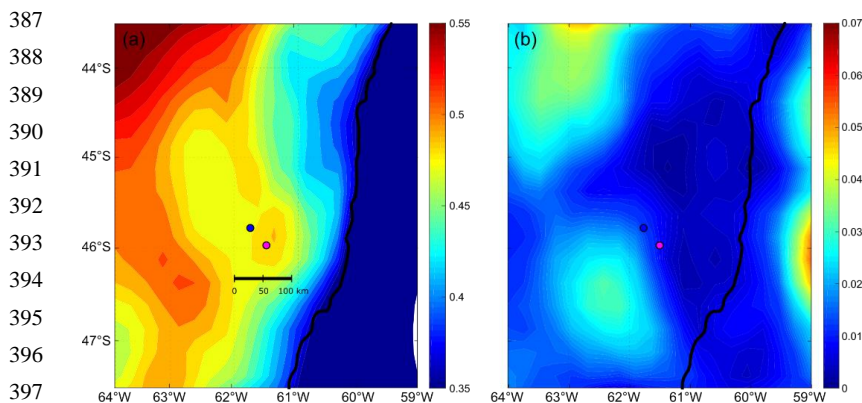
374

375 The mean and standard deviation of the ADT during the sampling period (16 to 28 November, 2021) evidenced a mesoscale  
376 anticyclonic eddy of about 100 km in diameter in the area where the Amphidomataeae bloom was observed at the two  
377 sampling locations (**Fig. 8**). In addition, the modelled trajectory of the particles released along the zonal transect at 46°S on  
378 November 10 showed high retention at the blooming area over the continental shelf after running for 20 days. On the contrary,  
379 high advection within the flow of the Malvinas Current was evidenced (**Fig. 9**). Notably, in the eddy area, particles slightly  
380 displaced southwards, remaining trapped in the area after 20 days since their release. The particles advected by geostrophic  
381 velocities suggest that the anticyclonic eddy acted as a potential mechanism to retain the Amphidomataeae bloom within the  
382 same location during the two synoptic samplings (**Fig. 9**). All the other particles released East and West of the eddy displayed



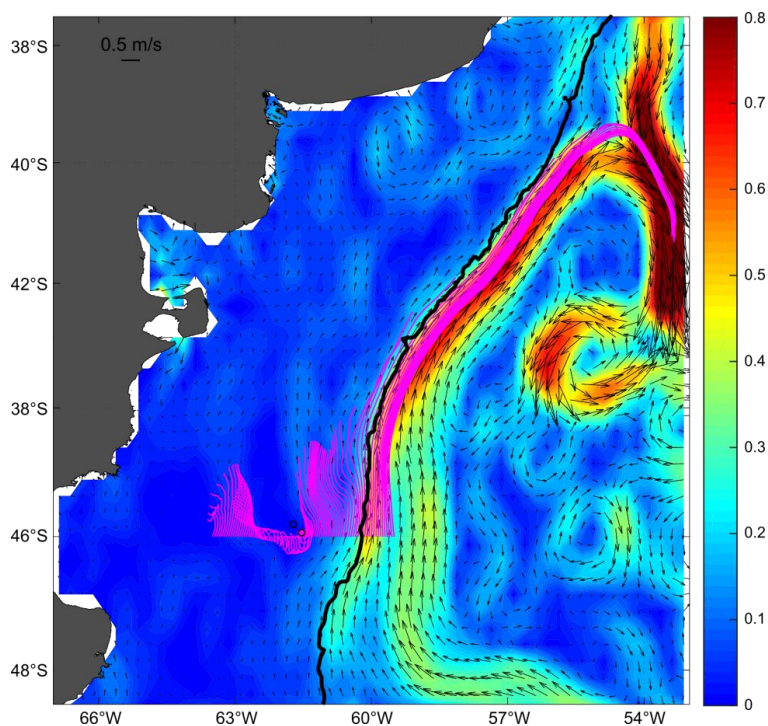


383 a different behaviour (**Fig. 9**), also shown in the **Appendix D** where four parcels of particles were advected from 16 to 25  
 384 November. West of the eddy they were advected northward at rather slow speed (average 5 cm/s) while East of the eddy they  
 385 increased their speed towards the north as they approached the continental slope. Within the core of the Malvinas Current,  
 386 speeds were as large as 80 cm/s (**Fig. 9**).



387  
 388  
 389  
 390  
 391  
 392  
 393  
 394  
 395  
 396  
 397  
 398 **Figure 8: (a) Mean and (b) standard deviation (std) of the Absolute Dynamic Topography (ADT, in meters) displayed**  
 399 **in colour scale, during the period November 16 to November 28, embracing the sampling period on both bloom stations:**  
 400 **GA01 (pink dot, Gayoso cruise) and AA09 (blue dot, Agujero Azul cruise).**

401

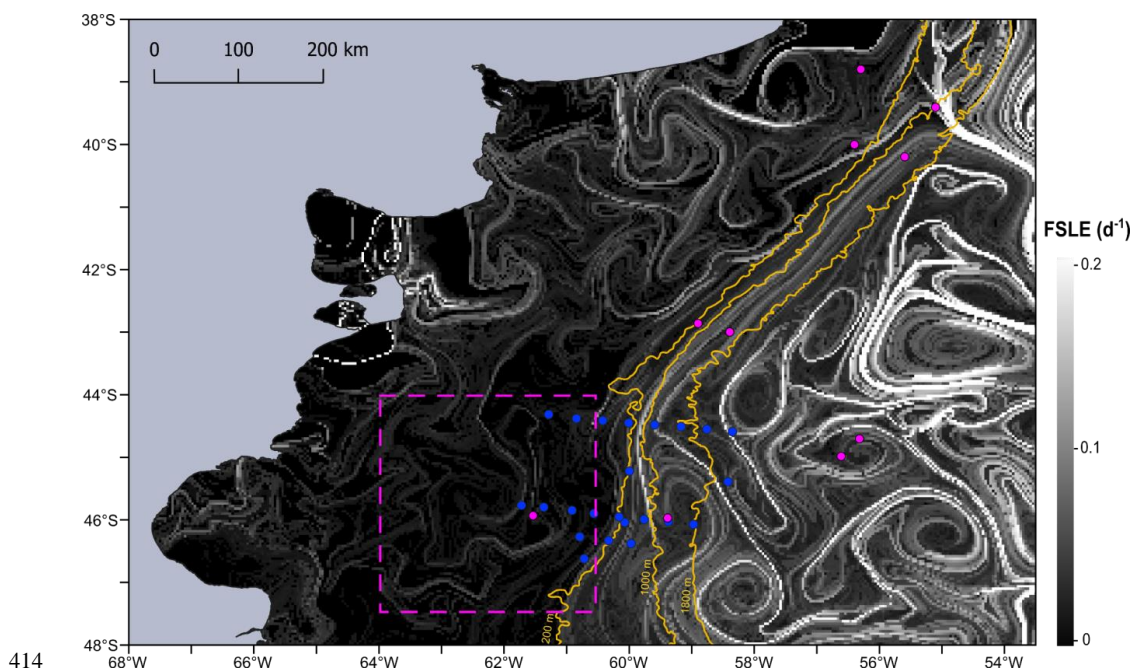


402  
 403 **Figure 9: Particle advection after 20 days since particle release on November 10, 2021. Initial points: one particle every**  
 404 **0.05 grades along 46°S. Note the high retention and the distinct behaviour of particles in the area of the sampling**  
 405 **stations: GA01 (pink dot) and AA09 (blue dot). Satellite altimetry geostrophic velocities averaged for the same 20 days**  
 406 **are also displayed with black vectors; the magnitude of the averaged speeds is represented with colours in the**  
 407 **background (m/s).**



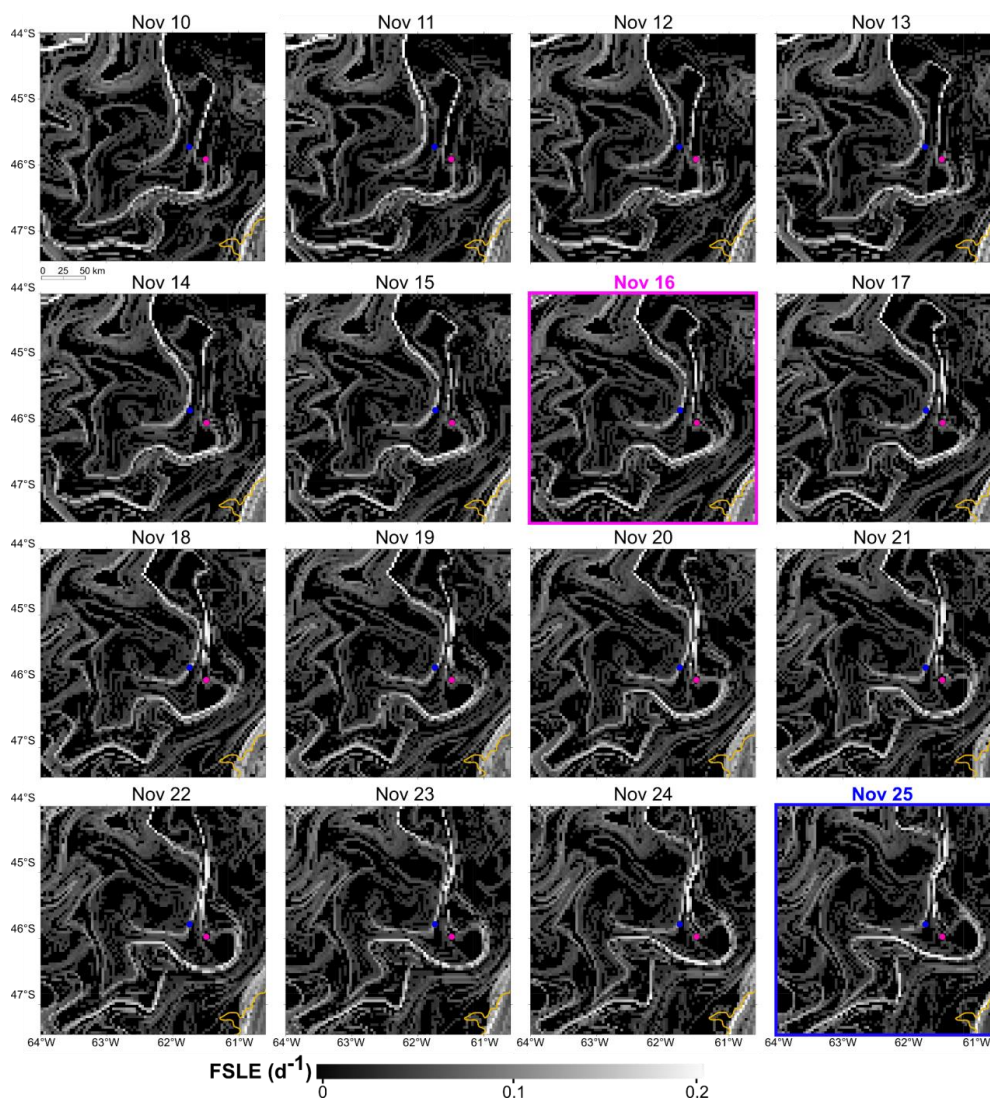


408 Moreover, the finite-size Lyapunov exponent (FSLE) ridges highlighted the stirring and hydrologically complex nature of the  
409 Southwestern Atlantic Ocean, associated with the high hydrographical heterogeneity of the oceanic waters (**Fig. 10**). Although  
410 FSLE were less intense over the shelf than in the adjacent oceanic waters, in the area where the Amphidomataceae bloom was  
411 sampled (pink dashed square in **Fig. 10**), two relatively strong FSLE ridges consistently kept both bloom stations within the  
412 same water mass during the period between the two synoptic samplings (**Fig. 11**).  
413



414  
415  
416 **Figure 10: Fronts identified as Finite-size Lyapunov Exponent (FSLE) ridges computed for November 16, shown**  
417 **against a grayscale background. All sampling stations from the Gayoso cruise (pink dots) and Agujero Azul cruise**  
418 **(blue dots) are indicated. November 16 corresponds to the sampling of the Amphidomataceae bloom at station GA01**  
419 **(pink dot within the square marked by a dashed pink line). The square highlights the area shown in Fig. 11.**

420  
421



422

423

**Figure 11: Finite-size Lyapunov Exponent (FSLE) ridges in the area of the two locations with the Amphidomataceae bloom: GA01 (pink dot) sampled on November 16, and AA09 (blue dot) sampled on November 25. See the Video of these daily images in the Appendix D. The 200 m isobath is indicated in yellow.**

426

427

#### 4. Discussion

428

429

##### 4.1. Amphidomataceae blooms in the Patagonian shelf

430

431

The phytoplankton spring and summer blooms in the Patagonian shelf display a southward progression related to the seasonal thermal cycle. In early spring (September-October), the water column stratifies north of ~45°S, favouring the proliferation of opportunistic micro-diatoms in the nutrient-rich, well-lit surface layers (Ferronato et al., 2023). South of ~45°S, the bloom initiates later in spring-early summer (December-January) and continues until autumn (March) (revised in Gunder et al., 2024). Here, blooms of nanoflagellates and dinoflagellates are triggered by combined vertical stability and nutrient-depleted surface waters (especially silicates) after the early-spring blooms of large diatoms (Balch et al., 2014; Carreto et al., 2016;

436



437 Ferronato et al., 2024). The massive proliferation of Amphidomataceans in mid-November 2021 was in line with this  
438 successional pattern. These nano-dinoflagellates bloomed in a stratified water mass with a deep mixed layer depth (~60 m).  
439 While dinoflagellates are less effective at nutrient resorption compared to diatoms, they can move throughout the stable water  
440 column to find light and nutrients (Glibert, 2016), especially at low phosphate levels (Lin et al., 2016) as observed at the  
441 stations GA01 and AA09 with high nitrate-to-phosphate ratios.

442 The success of the multispecific bloom of Amphidomataceae may be attributed to a combination of multiple intrinsic and  
443 extrinsic factors. For instance, their small cell-size, unique swimming modes and the production of azaspiracids may have  
444 alleviated grazing pressure (Tillmann et al., 2019). In fact, in the fixed samples, it was observed that many cells were obviously  
445 active and undergoing cell division and that these nanoflagellates were overwhelmingly the predominant photosynthetic  
446 protists responsible for the high chl-*a* levels, with negligible abundance of micro-grazers accompanying the bloom  
447 development. The presence of less than 2% of other protists (mixotrophs and heterotrophs) could be also related to a delay in  
448 the recovery of predators following the early blooms of microdiatoms, as well as to an abrupt development of the  
449 Amphidomataceae bloom, which may have prevented micrograzers from taking advantage of the available food. Another  
450 observation supporting the active persistence of the bloom was the pristine condition of the microenvironment surrounding the  
451 dense populations of Amphidomataceae (see **Appendix C**), with no aggregates or mucus formation typically observed in the  
452 late stages of blooms (Genitsaris et al., 2021). Furthermore, no competitors for light and nutrients were detected in the samples;  
453 specifically, no diatoms were found during microscopic examination. This may explain the rapid recovery of silicates (from 5  
454 to 22  $\mu\text{M}$ ) over the 10-day persistence of the Amphidomataceae bloom, as these silicates were not being utilised by silicate-  
455 requiring species. A similar observation was noticed during a bloom induced by iron-fertilization in the Southern Ocean, where  
456 diatoms predominated and silicate levels decreased from 10 to 6  $\mu\text{M}$  within the bloom patch over the course of 12-days  
457 (Abraham et al., 2000).

458

#### 459 **4.2. Highest abundance ever recorded for a bloom of Amphidomataceans**

460

461 With 17 described species of *Azadinium* and 14 of *Amphidoma*, the Amphidomataceae represent a small but diverse group of  
462 dinoflagellates. Most of these species are very similar in size and shape, which makes the qualitative identification and, in  
463 particular, the species specific quantification in field samples difficult. Hence, characterising the cryptic species of the  
464 multispecific bloom of Amphidomataceae in this study represented a major challenge, where a reliable species identification  
465 was achieved by the combination of several diagnostic details using electron microscopy. Light microscopic counting of fixed  
466 samples provided high quantitative accuracy, but reliable species identification was only possible in a few cases.  
467 Complementing the identification by microscopy with metabarcoding specifically targeting the internal transcribed spacer  
468 (ITS1) region (Liu et al., 2023), allowed for the detailed characterization of Amphidomatacean species diversity in the field  
469 samples. By combining the three approaches we were able to identify ribotypes and the toxic species, including previously  
470 described Amphidomataceae species for the Argentine Sea (Fabro et al. 2019; Tillmann et al., 2019; 2021) or species still  
471 undescribed in the global seas (see the **Appendix A**).

472 In the North Atlantic, AZA-1 (and its producing species, *Az. spinosum* ribotype A), has been identified as one of the most  
473 prevalent toxins among a wide range of AZA variants (Tillmann et al. 2021). Bloom density of Amphidomataceae around  
474 Ireland have been reported as  $8.3 \times 10^4$  cells  $\text{L}^{-1}$  for *Az. spinosum* (Wietkamp et al. 2020) and  $47 \times 10^5$  cells  $\text{L}^{-1}$  for *Amphidoma*  
475 *languida* (McGirr et al. 2022) and a small bloom of *Am. languida* in the North Sea with  $1.2 \times 10^5$  cells  $\text{L}^{-1}$  has also been described  
476 (Wietkamp et al. 2020). In this region, cases of human intoxication with azaspiracids have been linked to the consumption of  
477 contaminated mussels from the Irish West coast, where blooms in the shelf-break area can reach coastal shellfish beds through  
478 wind-driven advection (Raine, 2014). Notably, in the Argentine Sea, only AZA-2 has been detected in field and culture samples



479 (Turner and Goya, 2015; Fabro et al., 2019; Tillmann et al., 2019; Guinder et al., 2020), and so far, no poisoning events have  
480 been attributed to AZAs.

481 In this study, relatively high levels of solely AZA-2 were detected in bloom samples. A toxin profile of solely AZA-2 is up to  
482 now only known for the Argentine strain H-1-D11 of *Azadinium spinosum* ribotype B (Tillmann et al., 2019), and this ribotype  
483 was also identified in the present bloom. Relating AZA quantities to the relatively low abundance (0.1 to 0.4 % of total  
484 Amphidomataceae) of *Az. spinosum* ribtype B revealed AZA-2 cell quotas of 17-42 fg per cell, which is an order of magnitude  
485 higher than the cells quota of 2 to 9 fg per cell for strain H-1-D11 grown under laboratory conditions (Tillmann et al. 2019). In  
486 fact, *Az. spinosum* of ribotype A producing AZA-1 and -2 is the primary causative agent of AZA poisoning in Europe  
487 (Tillmann, 2018). However, the large majority of cells of *Az. spinosum* in the present bloom sample is from ribotype C, which  
488 is, based on analyses of several strains from Argentina, non-toxicogenic (Tillmann et al 2019), and all globally available strains  
489 (including strains from Argentina) of the other co-dominant species in the bloom, *Az. dalianene*, (Tillmann et al., 2019), also  
490 do not produce azaspiraides. In the Chilean continental shelf in the SE Pacific, AZAs have been detected in scallops and mussels  
491 (López-Rivera et al., 2010), but no intoxication events or large blooms of this clade have been documented. Moreover, only  
492 *Az. poporum* has been described as an AZA producer in Chilean waters (Tillmann et al., 2017a). Likewise in Peru, a relatively  
493 high bloom (up to one million cells per liter) of *Az. polongum* was detected in the summer of 2014, with no AZA production  
494 (Tillmann et al., 2017b). Although the continental shelves of Chile-Perú and Argentina have different hydrology, both span  
495 similar latitudinal gradients along the South American coasts and are influenced by the Humboldt and Malvinas Currents,  
496 which share a common origin in the Circumpolar Antarctic Current. Strikingly, both shelves exhibit different populations of  
497 Amphidomataceae, despite the expectation that ocean currents could serve as transport pathways for HAB species, promoting  
498 their dispersion (Giddings et al., 2014).

499

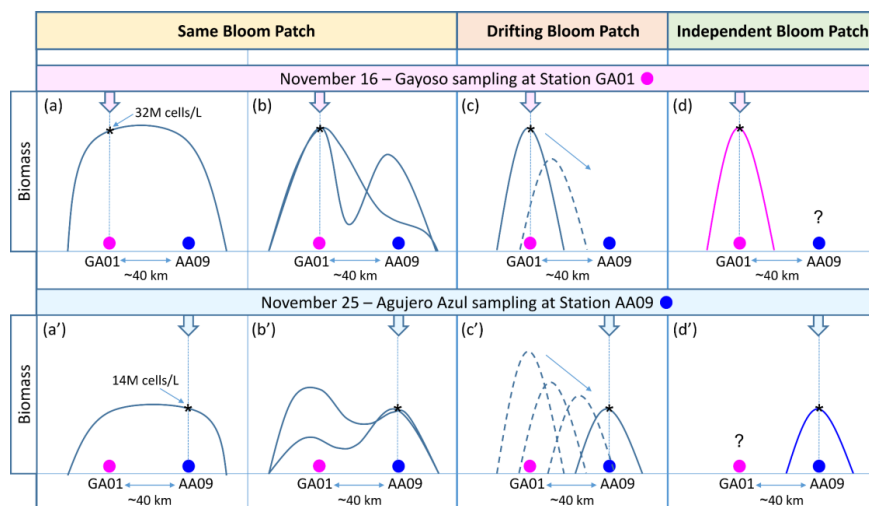
#### 500 **4.3. Spatio-temporal evolution of the bloom: retention and stirring**

501

502 Phytoplankton bloom initiation, magnitude, and persistence rely on a host of biogeochemical and physical processes. As  
503 discussed in previous sections, the explosive onset of the bloom of multiple species of Amphidomataceae was associated with  
504 a combination of water column stability, the negligible presence of micrograzers, and the ecological traits of this group that  
505 facilitate massive proliferation. However, these conditions alone do not fully explain the persistence of this bloom, which was  
506 sampled 10 days later at a location 40 km away in the offshore waters of the Patagonian shelf, where strong surface currents  
507 were expected to disperse plankton blooms. The persistence of this extraordinary bloom, characterized by its remarkable  
508 magnitude and consistent species composition, indicates the retention and accumulation of the bloom patch within the same  
509 water mass. In addition to the biological evidence confirming the presence of the same Amphidomataceae bloom at both  
510 sampling stages, analyses of circulation through altimetry, particle experiments, and FSLE—an indicator of frontal activity  
511 and stirring intensity—support the conclusion that the same bloom patch was captured at both locations. Two potential  
512 scenarios could explain this: (1) the same patch remained in the area over the ten days of sampling, occupying a space of 40  
513 km or larger (Fig. 12a and b), or (2) a smaller bloom patch was initially detected at station GA01 and then transported by  
514 stirring towards AA09 (Fig. 12c). A less likely scenario is that (3) two Amphidomataceae blooms developed independently at  
515 both locations (Fig. 12d). This situation is improbable due to the complex physical-biological interactions that drive different  
516 bloom developments, such as variable stirring (Abraham et al., 2000; Lehan et al., 2007; Della Penna et al., 2015) and changing  
517 environmental conditions that select for different species and functional groups across diverse spatio-temporal scales (Levy  
518 et al., 2018; Hernández-Carrasco et al., 2020; Mangolte et al., 2023). Moreover, no dormant cysts of Amphidomataceae are  
519 known, which could explain population outbreaks in specific locations, as observed in frontal areas for other dinoflagellates  
520 forming HABs (Smayda, 2002; Akselman et al., 2015).

521





522

523

524

525

526

527

528

529

530

531

532

533

534

535

536

537

538

539

540

541

542

543

544

545

546

547

548

549

550

551

**Figure 12: Hypothetical scenarios of the spatio-temporal evolution of the Amphidomataceae bloom during the 10-day period between the synoptic sampling at the two stations 40 km apart: GA01 (pink circle) and AA09 (blue circle). The bloom's biomass was 32 million cells  $L^{-1}$  at GA01 and 14 million cells  $L^{-1}$  at AA09. In the Same Bloom Patch (a-a' and b-b'), the bloom covered an area encompassing both sampling stations. The bloom developed such that the biomass was either distributed homogeneously across the patch (a-a') or heterogeneously (b-b'), resulting in variable biomass patterns over time and space. In the Drifting Bloom Patch (c-c'), the water mass with the Amphidomataceae bloom detected at station GA01 was transported by currents towards station AA09, where the bloom was detected with lower biomass but still with high intensity. The Independent Bloom Patch (d-d') suggests that two discrete, autonomous Amphidomatacean blooms developed locally at each sampling station.**

Additionally, the hydrographically complex Southwestern Atlantic creates a variety of microhabitats at the meso- and submesoscale. These include areas of upwelling, downwelling, eddies, retention, and dispersion (Becker et al., 2023; Beron-Vera et al., 2020; Salyuk et al., 2022; Saraceno et al., 2024). This spatial heterogeneity enhances the development of variable nutrient patches and phytoplankton productivity (Lehahan et al., 2017; Levy et al., 2018; Hernández-Carrasco et al., 2020; Ser-Giacomi et al., 2023). During the Gayoso cruise, contrasting phytoplankton assemblages and bloom types were observed at all sampling locations, including distinct blooms of dinoflagellates, coccolithophores, diatoms, and nanoflagellates. These variations were related to substantial heterogeneity in surface velocities and environmental conditions across the region (Ferronato et al., 2024). In this study, while the retention of the Amphidomataceae bloom is certainly limited by the accuracy of satellite altimetry maps, the documented 100 km diameter of the eddy is a reasonable size that can be distinguished using the gridded satellite altimetry maps produced by CMEMS. Although this retention is transient, this particular circulation facilitated the massive development of the Amphidomataceae bloom, with no evidence that this patch was advected through the Malvinas Current, as observed with drifters released east of the bloom area in spring 2021 (Saraceno et al., 2024). Our results highlight the importance of studying the evolution of phytoplankton blooms on continental shelves, focusing on the bio-physical coupling that drives their patchy nature, persistence, and transport, in order to capture short-lived blooms and their potential to cause toxic outbreaks.

Overall, this study is unique from both biological and physical perspectives due to the following factors: (i) the Amphidomataceae bloom observed in spring 2021 in the Argentine Sea, with up to 32 million cells per litre, represents the largest bloom of this clade ever recorded globally; (ii) unusual sampling in offshore shelf waters with two vessels over a ten-day interval allowed for synoptic observations of the bloom at two active developmental stages; (iii) simultaneous ecological





552 characterization of the bloom and surface currents and fronts provided insights into patch stirring and the short-term evolution  
553 of the bloom; (iv) field quantitative abundance data for Amphidomataceae are rare, and to our knowledge, this is the first  
554 detailed description of species abundance in field samples, combining light microscopy, electron microscopy, and  
555 metabarcoding; (v) the relatively low abundance of *Azadinium spinosum* Ribotype B indicated high AZA-2 cell quotas; (vi)  
556 the fine-taxon assessment of the Amphidomataceae bloom revealed biogeographical patterns and strain-specific toxic  
557 potential; and (vii) the use of interdisciplinary approaches sheds light on the bio-physical coupling underlying the persistence  
558 and horizontal transport of this extraordinary bloom in offshore shelf waters.

559

## 560 Appendix A

561

### 562 A1. Estimation and categorization of Amphidomatacean species diversity

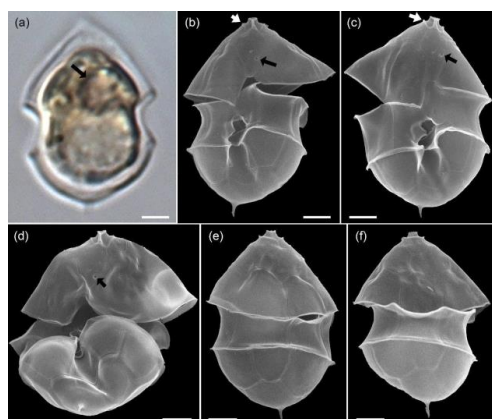
563 For the present study, we combined light microscopy (LM) quantification, scanning electron microscopy (SEM) examination,  
564 and metabarcoding to characterize the field samples as accurately as possible, both qualitatively and quantitatively. Generally,  
565 the following species of Amphidomataceae were identified:

566

#### 567 A1.1. *Azadinium spinosum*

568 Specimens were identified with SEM as *Az. spinosum* based on the combination of (1) presence of an antapical spine, and (2)  
569 presence of a ventral pore located on the right side of the suture of Plate 1' and 1" (Fig. A01). The vast majority of cells thus  
570 identified as *Az. spinosum* had a somewhat broader cell shape. Generally, identification of *Az. spinosum* is complicated as there  
571 are several different ribotypes (Tillmann et al., 2021), which notably differ in azaspiracid toxin presence and profile. In a  
572 previous study from the Argentine shelf region, it was shown that 23 out of 24 isolated strains of *Az. spinosum* were assigned  
573 to the non-toxicogenic ribotype group C, and cells from these strains also had a somewhat broader cell shape (Tillmann et al.,  
574 2019). Metabarcoding of the present bloom sample revealed that the most common sequences showed a high match with  
575 sequences of these Argentine ribotype C strains. A dominance of non-AZA-producing *Az. spinosum* (ribotype C) also aligns  
576 with the finding that no AZA-1, the marker toxin of the toxicogenic *Azadinium spinosum* ribotype A strains (Tillmann et al.,  
577 2021), was detected in the field samples. In the quantitative light microscopy (LM) counts, all medium-sized cells (length >  
578 12  $\mu\text{m}$ ) with a rounded hypotheca and an antapical spine were thus categorized as *Azadinium spinosum* ribotype C.

579



580

581 **Figure A01: LM (a) and SEM (b-f) of cells of the Amphidomatacean bloom stations identified as *Azadinium spinosum***  
582 **ribotype C. (b–d) Cells in ventral view. (e, f) Cells in dorsal view. Note the pyrenoid (black arrow in a), the position of**  
583 **the ventral pore (black arrows in b, c, d), the rim around the pore plate (white arrows in b, c) and the distinct antapical**  
584 **spine. Scale bars = 2  $\mu\text{m}$ .**

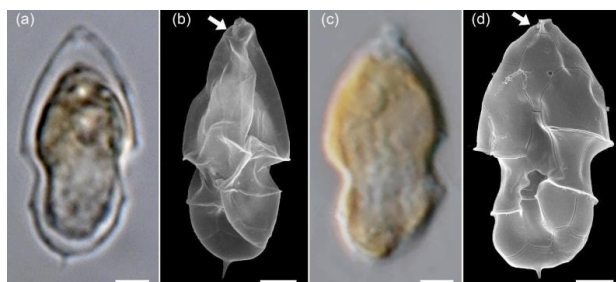


585

586 Recent studies have revealed the presence of a new, molecularly distinct species of *Azadinium* in the North Atlantic, which is  
587 morphologically indistinguishable from *Az. spinosum* and is currently provisionally referred to as *Azadinium cf. spinosum*  
588 (Tillmann et al., 2021). Therefore, it cannot be ruled out that this species was also present in the samples, but metabarcoding  
589 showed no evidence of the presence of *Az. cf. spinosum* in the bloom samples.

590 In addition to these broader cells of *Az. spinosum* ribotype C cells, LM analysis revealed a (much rarer) presence of distinctly  
591 slender cells with an antapical spine (Fig. A02a). Such cells perfectly correspond to cell shape of a single strain H-1-D11 from  
592 Argentina identified as a ribotype B strain of *Az. spinosum* (Tillmann et al., 2019), and this strain is depicted here for comparison  
593 (Fig. A02c, d). In SEM, specimen of slender shape lacked the rim around the pore plate (Fig. A02b), which is the morphological  
594 diagnostic feature differing in ribotype B strains from ribotype A and C strains, which all have a thick rim. Additionally,  
595 metabarcoding showed conformity of some sequences with other ribotype B *Az. spinosum* strains (e.g. 99% similarity with the  
596 Argentinean strain H-1-D11). Consequently, all slender cells with an antapical spine quantified in LM were categorized here  
597 as *Az. spinosum* ribotype B. Strain H-1-D11 from Argentina was shown to produce solely AZA-2 (Tillmann et al., 2019). As  
598 this was the only AZA detected in our field sample, this is additional support for this *Az. spinosum* ribotype B designation.

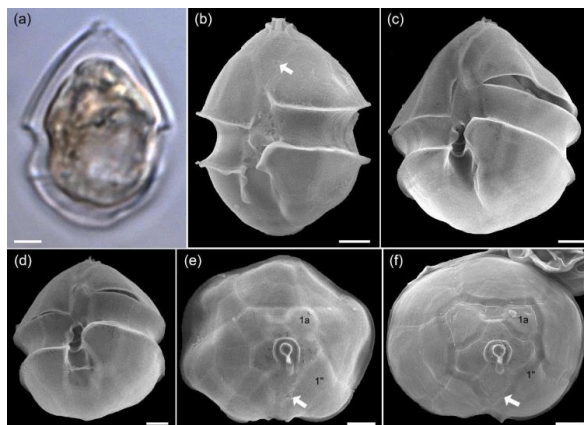
599



600

601 **Figure A02: LM (a), and SEM (b) of cells of the amphidomatacean bloom stations identified as *Azadinium spinosum*.**  
602 **For comparison, LM (c) and SEM (d) of cells of strain H1-D11 of *Azadinium spinosum* ribotype B isolated from the**  
603 **Argentine shelf in 2015. Note the elongated cells shape, the distinct antapical spine, and the lack of a rim around the**  
604 **pore plate (white arrows in b and d). Scale bars = 2  $\mu$ m.**

605



606

607 **Figure A03: LM (a) and SEM (b-f) of cells of the Amphidomatacean bloom stations identified as *Azadinium obesum*.**  
608 **(b–d) Cells in ventral view. (e, f) Epitheca in apical view. Note the lack on an antapical spine, the position of the ventral**  
609 **pore (white arrows in b, e, f) and the lack of contact between Plates 1a and 1'' (kofoidian plate label notation) visible in**  
610 **e) and f). Scale bars = 2  $\mu$ m.**

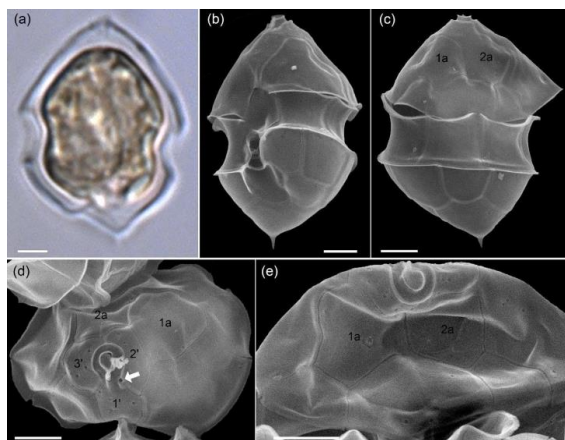


611

### 612 A 1.2. *Azadinium obesum*

613 Cells of the non-toxigenic species *Az. obesum* were identified in the SEM samples based on the combination of the following  
614 features: (1) no antapical spine, (2) ventral pore on the right side of Plate 1', and (3) no contact between Plates 1a and 1'' (Fig.  
615 A03). All such cells had a distinctly broad oval shape and were relatively large. In the light microscope, all relatively large  
616 oval Amphidomataceae cells with a rounded hypotheca and no visible spine were therefore categorized as *Azadinium obesum*.

617



618

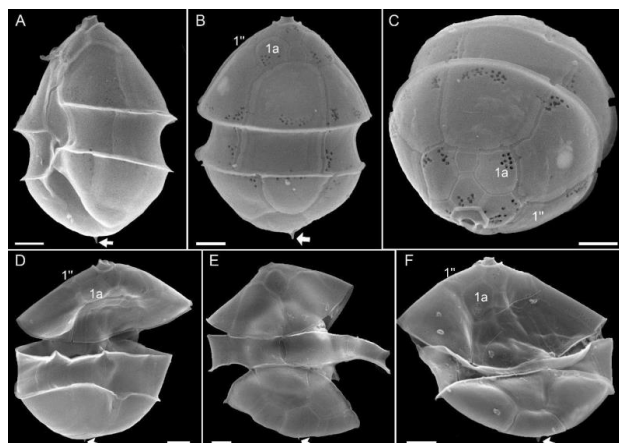
619 **Figure A04: LM (a) and SEM (b-f) of cells of the amphidomatacean bloom stations identified as *Azadinium dalianense*.**  
620 **(b) Cell in ventral view. (c) Cell in dorsal view. (d) Epitheca in apical view. (e) Epitheca in dorsal view. Note the distinct**  
621 **apical spine on a triangular bumpy hypotheca (a–c), the position of the ventral pore on the left side of the pore plate**  
622 **(white arrow in d), the presence of only two large anterior intercalary plates 1a and 2a (c–e) and presence of only 3**  
623 **apical plates in (d) (kofoidian plate label notation). Scale bars = 2 μm.**

624

### 625 A 1.3. *Azadinium dalianense*

626 With the rounded hypotheca, cells of *Az. obesum* and *Az. spinosum* ribotype C were clearly distinguishable in the light  
627 microscope from cells with a distinctly protruding bump, at the tip of which a small spine was present (Fig. A04a).  
628 Corresponding cells detected in SEM preparations (Fig A04b–e) were identified as *Az. dalianense*, based on the combination  
629 of the following features: (1) ventral pore on the left side of the pore plate, (2) asymmetrical hypotheca with a bump and a  
630 distinct antapical spine, and (3) presence of only 3 apical plates and 2 anterior intercalary plates. Since all three features were  
631 only rarely visible simultaneously due to the cell's orientation, the presence of the somewhat similar species *Az. perfusorium*  
632 cannot be ruled out. *Az. perfusorium* also has a posterior small bump with a spine and a ventral pore located on the left side of  
633 the pore plate, but it possesses 4 apical plates and 3 intercalary plates (Salas et al., 2021). However, neither the SEM nor  
634 metabarcoding provided any indication of its presence in the samples. The occurrence of *Az. dalianense* in the region is well  
635 documented by a series of strains isolated from the Argentine shelf in 2015 (Tillmann et al., 2019), and *Az. dalianense* was  
636 also identified as part of *Azadinium* blooms in 1991 (Tillmann and Akselman, 2016). Metabarcoding additionally indicated the  
637 presence of two different ribotypes of *Az. dalianense*, namely E and B as defined in Tillmann et al. (2019), where all previous  
638 strains from Argentina belong to the ribotype E clade. Accordingly, the majority of reads from the bloom station *Az. dalianense*  
639 were from ribotype E (represented by strains H-4-E8 and N-12-04 in the reference dataset), whereas reads of ribotype B  
640 (represented by strain IFR-ADA-01C) made only ca. 0.02 % of all *Az. dalianense* reads. All strains of *Az. dalianense*  
641 representing different ribotypes collected from various regions analysed so far were non-toxigenic.

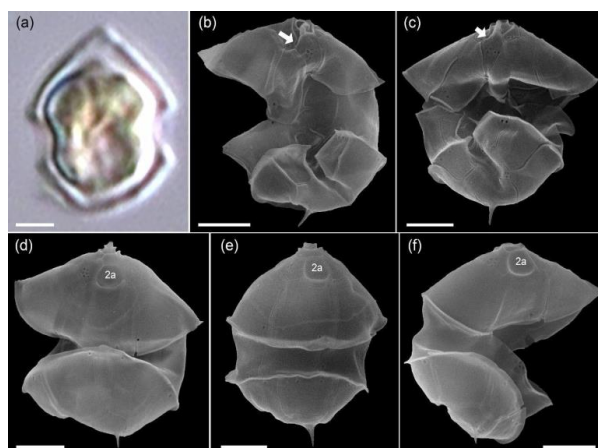
642



643  
644 **Figure A05: SEM of yet unidentified cells of *Azadinium* sp. 1 of the Amphidomatacean bloom stations. (a) Cell in left-**  
645 **lateral ventral view. (b) Cell in dorsal view. (c) Cell in apical view. (d–f) Cells in dorsal view. Note the small indistinct**  
646 **apical spine (white arrow in a, b, d–f) and the lack of contact between plates 1a and 1'' (kofoidian plate label notation)**  
647 **visible in b, c, d, f. Scale bars = 2 μm.**

648

649 The classification and quantification of *Az. obesum* and *Az. dalianense*, however, is complicated by the fact that a number of  
650 cells of an unclear assignment were found in the samples (Fig. A05). These cells, like *Az. obesum*, (1) had a ventral pore on  
651 the right side of Plate 1' and (2) no contact between Plates 1a and 1'', but unlike *Az. obesum*, they had a distinct, albeit small,  
652 antapical spine. This combination of features is not known from any described *Azadinium* species, suggesting that this may be  
653 a new species. However, for a complete description as a new *Azadinium* species, further investigations are necessary, ideally  
654 adding sequence data and analyses of toxin production. In any case, it is clear that cells of this type will have been included in  
655 the categories *Az. obesum* or *Az. spinosum* during the light microscope analyses and quantifications.



656  
657 **Figure A06: LM (a) and SEM (b–f) of cells of the Amphidomatacean bloom stations identified as *Azadinium***  
658 ***dexterporum*. (b, c) Cells in ventral view. (d–f) Cells in dorsal view. Note the small size, the distinct antapical spine, the**  
659 **position of the ventral pore on the right side of the pore plate (white arrows in b, c), and the concave central intercalary**  
660 **plate 2a visible in d–f. Scale bars = 2 μm.**

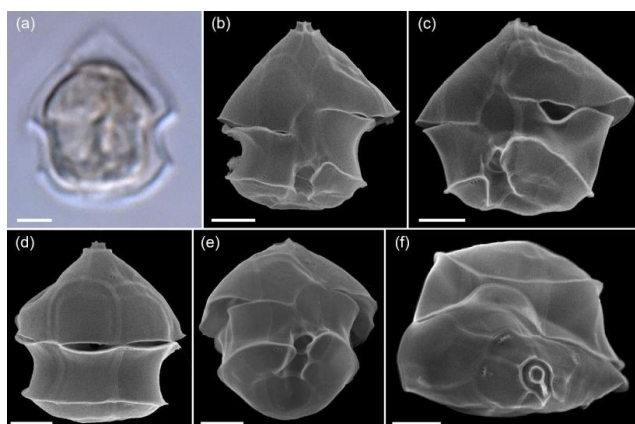
661

#### 662 **A 1.4. Smaller Amphidomatacean species: *Azadinium dexterporum*, *Amphidoma parvula*, and *Amphidoma languida***

663 While *Az. spinosum*, *Az. obesum*, and *Az. dalianense* fall into a slightly larger size class, a number of smaller *Azadinium* species



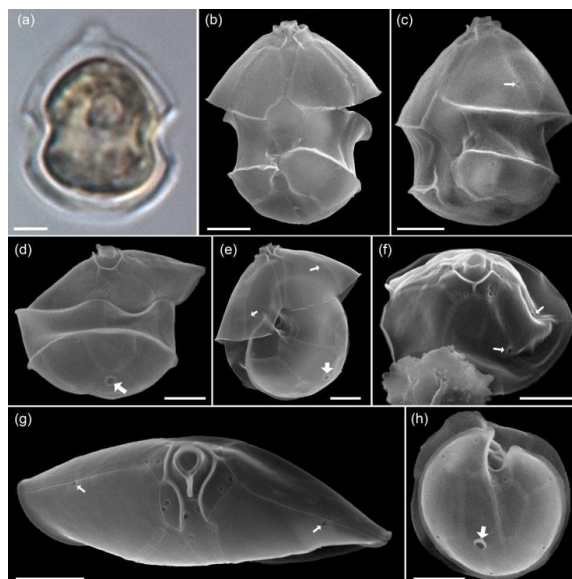
664 were identified and categorized in the samples. One of them was *Az. dexteroporum* (Fig. A06), which was identified in the  
 665 SEM by the following combination of features: (1) relatively small size, (2) presence of a distinct antapical spine, (3) a slightly  
 666 posteriorly positioned ventral pore on the right side of the ventral plate, and (4) a distinctly concave central intercalary Plate  
 667 2a. Metabarcoding revealed a number reads for an *Azadinium* sp. 1 with *Az. dexteroporum* as closest species suggestion (line  
 668 7 in Table S01), however only with rather low similarity (90-95%) compared to the reference database. Global wise, there are  
 669 only three available strains of *Az. dexteroporum*, and of those only one strain from the Mediterranean was identified as a  
 670 producer of AZA (Rossi et al. 2017). In contrast, two additional strains from the North Atlantic, which also had marked  
 671 sequence differences compared to the Mediterranean strain, did not produce AZAs (Tillmann et al. 2020). The low similarity  
 672 of *Az. dexteroporum* reads from the present bloom samples thus indicate that the local population may represent a new ribotype  
 673 quite distinct from the AZA-producing ribotype, and strain isolation of local *Az. dexteroporum* is needed to clarify its identity  
 674 and toxin production potential.  
 675



676  
 677 **Figure A07: LM (a) and SEM (b-f) of cells of the Amphidomatacean bloom stations identified as *Amphidoma parvula*.**  
 678 **(b, c) Cells in ventral view. (d) Cell in dorsal view. (e) Cell in ventral antapical view. (f) cell in apical view. Note the**  
 679 **small size, the flat hypotheca, the shape of the 1' plate visible in a, b, the group of pores in the second antapical plate**  
 680 **(white arrow in e), and the relatively long apical plates visible in d and f. Scale bars = 2  $\mu$ m.**

681  
 682 In the same size class, cells were also observed that were identified in SEM as *Amphidoma parvula* (Fig. A07) by (1) their flat  
 683 hypotheca and (2) a characteristically shaped 1' plate. This non-toxicogenic species was described in 2018 based on a culture  
 684 isolated from the Argentine shelf (Tillmann et al., 2018). In accordance, a low number of reads with high similarity to *Am.*  
 685 *parvula* strain H-1E9 (>98 %) recorded by metabarcoding. With its relatively long apical plates, *Am. parvula* could also be  
 686 easily distinguished in the SEM from the similarly small *Am. languida*, which was also identified in SEM (Fig. A08). In *Am.*  
 687 *languida*, (1) the small apical plates, and (2) the presence of a large characteristic antapical pore is a distinguishing feature.

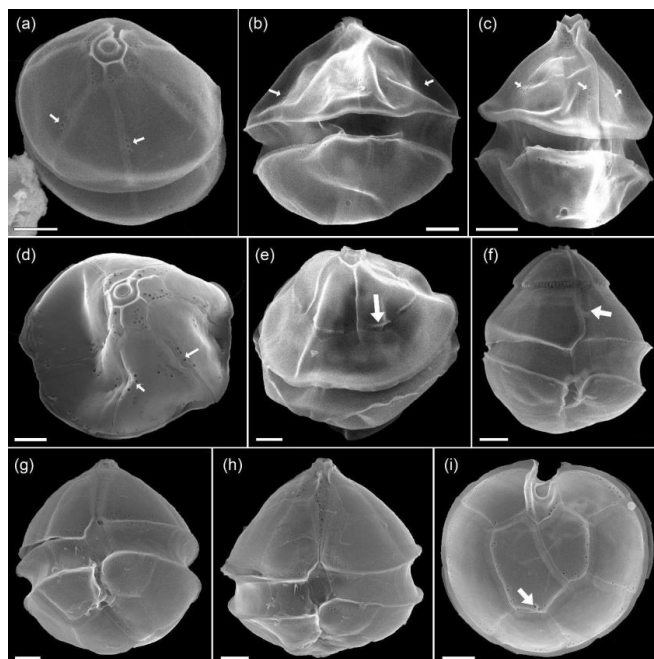




688  
689 **Figure A08: LM (a) and SEM (b-f) of cells of the Amphidomatacean bloom stations identified as *Amphidoma languida*.**  
690 **(b, c) Cells in ventral view. (d) Cell in dorsal view. (e) Cell with epitheca in ventral view and hypotheca in antapical**  
691 **view. (f) Epitheca in lateral apical view. (g) epitheca in apical view. (h) Hypotheca in antapical view. Note the shape of**  
692 **the 1' Plate visible in a), the distinct antapical pore in the second antapical plate (white arrows in d, e, h), and the**  
693 **relatively short antapical plates visible in d, f, g. Also note that there are only single pores on precingular plates (small**  
694 **white arrows in c, e, f, g). Scale bars = 2  $\mu$ m.**

695  
696 However, in 2024, a new species of *Amphidoma*, *Am. fulgens*, was described, which is morphologically almost identical to  
697 *Am. languida* but shows significantly different sequence data and, different to *Am. languida*, does not produce azaspiracids  
698 (Kuwata et al., 2024). *Amphidoma fulgens* was found to be widely distributed in the Pacific, but there are no records yet from  
699 the Atlantic Ocean. Despite its presence in the bloom samples, there were no reads related with higher similarities to *Am.*  
700 *languida* in the ITS metabarcoding data set, but only very few reads with rather low similarity to *Amphidoma* entries in the  
701 database. This seems to be in line with the general notion that ITS sequencing of cultured strains of *Am. languida* in many  
702 cases failed (Wietkamp et al. 2019). In fact, data of a previous metabarcoding study (Liu et al. 2023) showed that *Am. languida*  
703 hits were abundant in Chinese waters in the LSU dataset but absent in the ITS-1 data set. While *Am. languida* and also *Am.*  
704 *fulgens*, according to their original descriptions, only have one small pore on each precingular plate (Tillmann et al., 2012;  
705 Kuwata et al., 2024), there were also several cells of *Amphidoma* with three or more small pores on individual precingular  
706 plates (Fig. A09a–d). To what extent these cells represent *Am. languida* or other yet undescribed and closely related species,  
707 requires further clarification.

708



709

710 **Figure A09:** SEM of unidentified cells of *Amphidoma* spp. of the Amphidomatacean bloom stations. (a–d) Cells in apical  
711 (a, c) or dorsal (b, c) view resembling *Amphidoma languida*, but with multiple pores in precingular plates (small white  
712 arrows in a–d). (e) A cell of *Amphidoma* sp. in dorsal view. Note the very long apical plates. The row of pores with a  
713 distinct rim on the apical plates (white arrow in e) resemble *Amphidoma alata*. (f) Cell of an unidentified *Amphidoma*  
714 sp. 1 in ventral view. Note the long apical plates, the ventral depression (white arrow in f), and the row of pore on the  
715 posterior suture of apical plates. (g, h). Two cells of *Amphidoma* sp. resembling *Amphidoma trioculata*. (i) Hypotheca in  
716 antapical view of an unidentified *Amphidoma*. Note the multiple pores on the plates and the presence of a very small  
717 antapical pores on the second antapical plate (white arrow in i). Scale bars = 2  $\mu\text{m}$ .

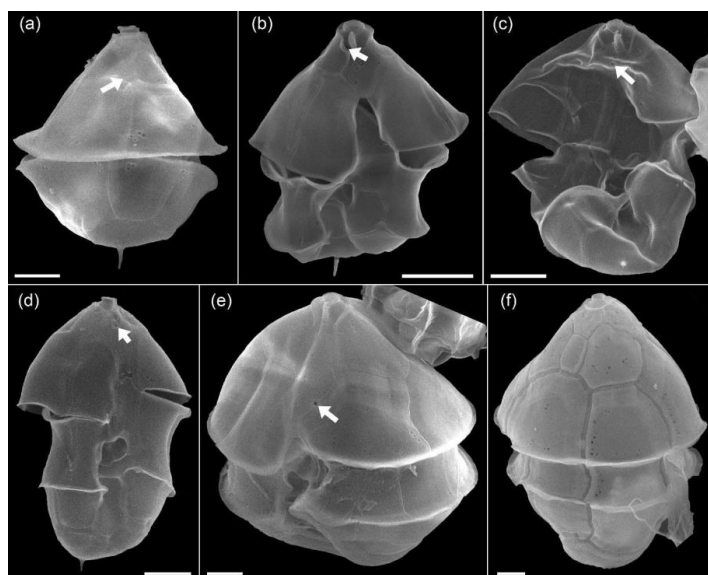
718

719 Due to the very similar size of *Az. dexteroporum*, *Am. parvula*, and *Am. languida*, all three species as identified with SEM are  
720 present in the one category of small amphidomatcean cells used for light microscopic analysis and quantification.

#### 721 A 1.5. Other Amphidomataceae

722 In the SEM, a few other cells were observed, which can also be assigned to the genus *Amphidoma*. The epitheca found in  
723 dorsal view in Fig. A09e with its characteristic pore ridges on the large apical plates corresponds to *Am. alata*, a species which  
724 was described from the Argentina shelf (Tillmann, 2018). The cell depicted in Fig. A09f in ventral view likely represents a  
725 new species of *Amphidoma*. The cells in Figs. A09g-i likely correspond to *Am. trioculata*, another species described from  
726 Argentina (Tillmann, 2018), though assigning the isolated hypotheca (Fig. A09i) is difficult.

727



728

729

730

731

732

733

734

735

736

737

738

739

740

741

742

743

744

745

746

747

748

749

750

751

752

753

754

755

**Figure A10: SEM of unidentified cells of *Azadinium* spp. of the Amphidomatacean bloom stations. (a) Cell in dorsal view. Note the very small and 5-sided intercalary plate (white arrow in a). (b) Cell of *Azadinium* sp. 1 in ventral view. Note the very short 1' Plate and the position of the ventral pore inside the pore plate (white arrow in b). It may be assumed but is not clear if (a) is the dorsal view of such an *Azadinium* sp. 1. (c, d), Two cells in ventral view of *Azadinium* sp. 2. Note the position of the ventral pore in apical position inside of Plate 1' (white arrows in c, d). (e) Cell of *Azadinium* sp. 3 in lateral ventral view. Note the position of the ventral pore (white arrow in e) and the rather long apical plates. (f). Dorsal view of an *Azadinium* sp. 4 resembling in size and shape *Azadinium asperum*. Scale bars = 2  $\mu$ m.**

Moreover, for a more complete description of the diversity of Amphidomataceae in the bloom sample, the following individual findings (Fig. A10) should also be mentioned: A cell in dorsal view (Fig. A10a) had a very distinct antapical spine, relatively large apical plates, and a small six-sided central intercalary plate. This combination of features has not been described in any known *Azadinium* species, suggesting that this may represent a new species. The cell depicted in Fig. A10b had a distinct antapical spine, a ventral pore on the right side of the pore plate, and a very short first apical plate, with the anterior sulcal plate extending far into the epitheca. Both cells in Figs. A10b and c resemble *Az. spinosum* but differ in that the ventral pore is centrally located within Plate 1' in the apical area. They likely correspond to the cells designated as *Azadinium* sp. 3 in Fig. 14 b, c, in Tillmann (2018). The cell in Fig. A10e had a ventral pore on the right side of Plate 1' (like *Az. spinosum* and *Az. obesum*), but here the lateral apical plates were significantly larger than in these species. The cell in Fig. A10f in dorsal view in terms of size and shape might correspond to *Az. asperum* described from the Argentine shelf (Tillmann, 2018), undoubtedly an *Azadinium* species due to the apical pore and intercalary plates, does not match any previously described species based on size (ca 20  $\mu$ m cell length) and shape. This, along with the other cells in Fig. A09 which likely represents previously undescribed species due to the unique combination of features, highlights the great diversity of Amphidomataceae in this 2021 bloom sample.

## Appendix B

### Species diversity based on ITS1-based metabarcoding



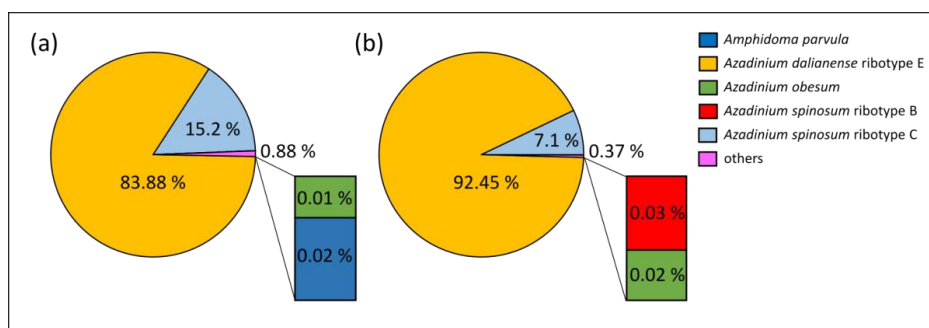
756 **Table B01: Species detected by Amplicon Sequence Variant (ASV) reads at stations GA01 and AA09.**

757

Nr	species	Genbank	Identity %	GA01	AA09
1	<i>Amphidoma parvula</i>	KY996792	>98	19	0
2	<i>Amphidoma</i> sp. 1	OQ360107	90-95	158	200
3	<i>Amphidoma</i> sp. 2	LC788745	90-95	16	0
5	<i>Azadinium dalianense</i> ribotype E	LS974150	90-95	41	63
			95-98	33	58
			>98	93,775	98,503
6	<i>Azadinium dalianense</i> ribotype B	MF033117	95-98	9	0
			>98	0	19
7	<i>Azadinium</i> sp. 1	OQ360091	90-95	36	41
8	<i>Azadinium</i> sp. 2	OQ360094	>98	6	5
9	<i>Azadinium spinosum</i> ribotype C	MK405512	>98	17,006	7,589
10	<i>Azadinium spinosum</i> ribotype B	LS974169	>98	0	37
11	<i>Ansanella</i> sp.	MN604385	90-95	4	13
12	<i>Bicheleria</i> sp.	KC895487	90-95	12	52
13	<i>Bicheleria cincta</i>	KC895487	>98	6	17
14	<i>Blastodinium oviforme</i>	JX473680	95-98	2	0
15	<i>Karlodinium decipiens</i>	LC521288	95-98	0	7
			>98	885	106
16	<i>Karlodinium digitatum</i>	MN133932	>98	3	0
17	<i>Kirithra asteri</i>	MW267275	>98	41	186
18	<i>Pelagodinium beii</i>	KP843723	>98	48	77

758

759



760

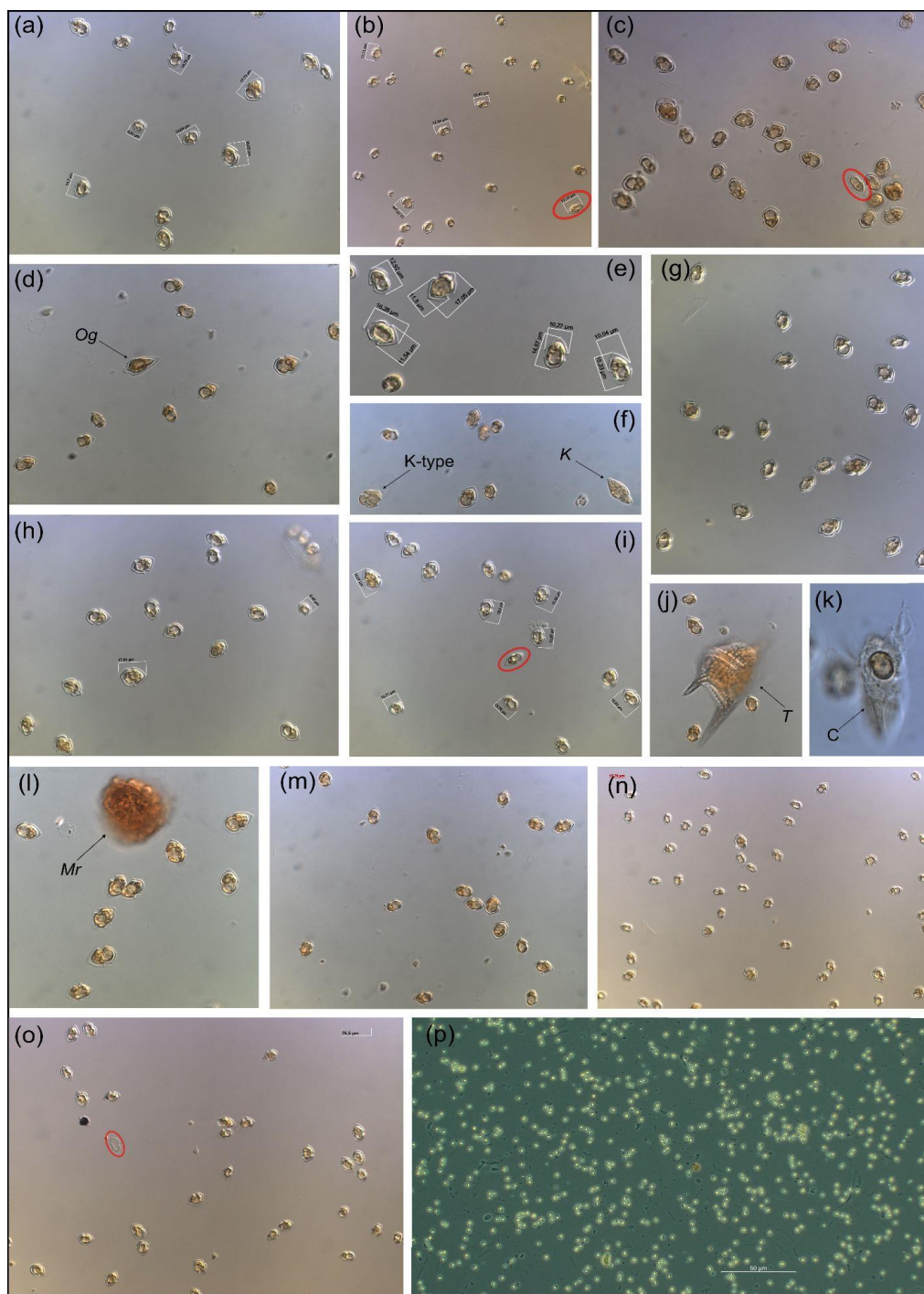
761 **Figure B01: Relative abundance (in %) of the Amphidomataceae species detected with metabarcoding targeting ITS1**  
 762 **regions at stations GA01 (a) and AA09 (b).**

763

764 **Appendix C**

765

766 **Overall appearance of the pure Amphidomataceae bloom in fixed field samples**



767

768

769

770

771

772

**Fig. C01:** Micrographs of the Amphidomataceae bloom taken under light microscopy at low magnification: 200x. Only (e) was taken under 400x and (p) was taken using fluorescence in 100x. The toxic species *Azadinium spinosum* ribotype B is indicated in a red circle. The arrows indicate other protists: *Og*: *Oxytoxum gracile*, *K-type*: Kareniacea-type cell, *K*: *Katodinium* sp., *T*: *Tripos* sp., *C*: ciliate with a cell of Amphidomataceae inside, *Mr*: *Mesodinium rubrum*.

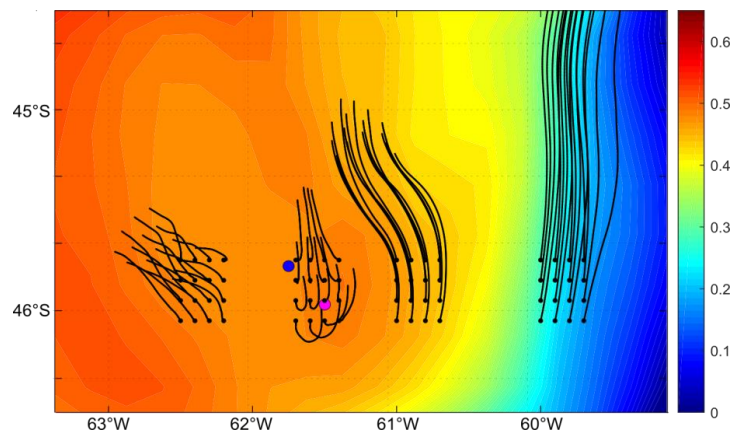




773 **Appendix D**

774

775 **Retention of particles in the blooming area**



776

777 **Fig. D01: Background colours: Absolute Dynamic Topography (m) averaged from 16 to 25 November. Black lines**  
778 **correspond to the advection of particles for the same period after release at the points indicated with a black dot on 16**  
779 **of November.**

780

781 **Supplementary material:** Video showing the daily evolution from 10 to 25 November 2021 of the Finite-size Lyapunov  
782 Exponent (FSLE) ridges in the area of the two locations with the Amphidomataceae bloom: GA01, pink dot, sampled on  
783 November 16, and AA09, blue dot, sampled on November 25. The two stations remained within the same water mass separated  
784 by two maxima FSLE.

785

786 **Data availability:** The CTD data and the abundance of protistan species counted under light microscopy at the sampling  
787 station GA01 and AA09, will be publicly available in the repository Pangaea Data Publisher ([www.pangaea.de](http://www.pangaea.de)). Data from  
788 the Gayoso cruise is available at: <https://doi.pangaea.de/10.1594/PANGAEA.971564>. Sequences obtained in this study are  
789 available in the National Center for Biotechnology Information, Sequence Read Archive (<http://www.ncbi.nlm.nih.gov/sra>).

790

791 **Author Contribution:** VAG conceptualised and designed the study, coordinated the planning and execution of field and  
792 laboratory work, and secured funding. VAG and UT analysed the plankton samples using LM and SEM. MR processed the  
793 satellite-derived chlorophyll data and the Lyapunov coefficients. CF and FR conducted field research and processed the CTD  
794 data. VAG and BK processed the toxin samples. HG processed the DNA samples. MS analysed the geostrophic currents and  
795 performed the particle tracking modelling. All co-authors contributed to the interpretation of the results. VAG prepared the  
796 manuscript with contributions from all co-authors.

797

798 **Competing interests:** The authors declare that they have no conflict of interest.

799

800 **Acknowledgments and Funding:** VAG and MS acknowledge the BioMMAr consortium and the common grant received  
801 from the Argentinean Initiative Pampa Azul (PIDT A6) to carry out the Gayoso cruise. VAG acknowledges the academic  
802 mobility projects: FitoxNorPat, CONICET-DAAD call-2020, and Coastcarb, H2020-Marie Skłodowska-Curie Actions,  
803 MSCA-RISE-2019, N° 872690. VAG especially thanks Marcelo Acha from INIDEP, Argentina, for his invitation to  
804 participate in the WG of the Marine Priority Area of Agujero Azul, from the Pampa Azul Initiative. VAG also thanks Annegret



805 Mueller and Thomas Max for their help and guidance in the laboratory work on processing toxin samples, UT and HG thanks  
806 Annegret Müller for DNA extraction. The authors thank the Argentinean authorities, the captain and crew of the RV Bernardo  
807 Houssay (Prefectura Naval Argentina) and the RV Victor Angelescu (INIDEP).

808

## 809 **References**

810

811 Abraham, E. R., Law, C. S., Boyd, P. W., Lavender, S. J., Maldonado, M. T., and Bowie, A. R. Importance of stirring in the  
812 development of an iron-fertilized phytoplankton bloom. *Nature*, 407(6805), 727-730, <https://doi.org/10.1038/35037555>, 2000.

813 Akselman, R., and Negri, R.M. Blooms of *Azadinium cf. spinosum* Elbrächter et Tillmann (Dinophyceae) in northern shelf  
814 waters of Argentina, Southwestern Atlantic. *Harmful Algae* 19, 30–38, <https://doi.org/10.1016/j.hal.2012.05.004>, 2012.

815 Akselman, R., Krock, B., Alpermann, T.J., Tillmann, U., Borel, C.M., Almandoz, G.O., and Ferrario, M.E. *Protoceratium*  
816 *reticulatum* (Dinophyceae) in the austral Southwestern Atlantic and the first report on YTX-production in shelf waters of  
817 Argentina. *Harmful Algae* 45, 40–52, <https://doi.org/10.1016/j.hal.2015.03.001>, 2015.

818 Alemany, D., Zavatteri, A., Prandoni, N., Giussi, A. R. Chapter 7: Fisheries in the Patagonian shelf break Front. In: The  
819 Patagonian shelf-break Front. Ecology, Fisheries, Wildlife Conservation. Acha, M., Iribarne, O., Piola, A. (Eds). Springer  
820 Nature. ISBN: 978-3-031-71189-3, 2024.

821 Almandoz, G.O., Cefarelli, A.O., Diodato, S., Montoya, N.G., Benavides, Carignan, M., Hernando, M., Fabro, E., Metfies, K.,  
822 Lundholm, N., Schloss, I.R., Alvarez, M., and Ferrario, M.E. Harmful phytoplankton in the Beagle Channel (South America)  
823 as a potential threat to aquaculture activities. *Mar. Poll. Bull.* 145, 105–117, <https://doi.org/10.1016/j.marpolbul.2019.05.026>,  
824 2019.

825 Anderson, C. R., Moore, S. K., Tomlinson, M. C., Silke, J., and Cusack, C. K. Living with harmful algal blooms in a changing  
826 world: strategies for modelling and mitigating their effects in coastal marine ecosystems. In: Coastal and marine hazards,  
827 risks, and disasters. Elsevier, ISBN: 978-0-12-396483-0, 495–561, 2015.

828 Anderson, D. M., Fensin, E., Gobler, C. J., Hoeglund, A. E., Hubbard, K. A., Kulis, D. M., Landsberg, J. H., Lefebvre, K. A.,  
829 Provoost, P., Richlen, M. L., Smith, J. L., Solow, A. R., Trainer, V. L., Marine harmful algal blooms (HABs) in the United  
830 States: history, current status and future trends. *Harmful Algae* 102, 101975, <https://doi.org/10.1016/j.hal.2021.101975>, 2021.

831 Balch, W. M., Drapeau, D. T., Bowler, B. C., Lyczkowski, E. R., Lubelczyk, L. C., Painter, S. C., Poulton, A. J. Surface  
832 biological, chemical, and optical properties of the Patagonian Shelf coccolithophore bloom, the brightest waters of the Great  
833 Calcite Belt. *Limnol. Oceanogr.* 59(5): 1715-1732, <https://doi.org/10.4319/lo.2014.59.5.1715>, 2014.

834 Becker, F., Romero, S. I., and Pisoni, J. P. Detection and characterization of submesoscale eddies from optical images: a case  
835 study in the Argentine continental shelf. *Int. J. Remote Sens.*, 44(10), 3146-3159,  
836 <https://doi.org/10.1080/01431161.2023.2216853>, 2023.

837 Beron-Vera, F.J., Bodnariuk, N., Saraceno, M., Olascoaga, M.J., Simionato, C. Stability of the Malvinas current. *Chaos* 30  
838 (1), 13152. <https://doi.org/10.1063/>, 2020.

839 Cadailon, A. M., Mattera, B., Albizzi, A., Montoya, N., Maldonado, S., Rey, A. R., Riccialdelli, L., Almandoz, G.O. and  
840 Schloss, I. R. Multispecies mass mortality in the Beagle Channel associated with paralytic shellfish toxins. *Harmful Algae*,  
841 132, 102581, <https://doi.org/10.1016/j.hal.2024.102581>, 2024.

842 Carreto, J. I., Montoya, N. G., Carignan, M. O., Akselman, R., Acha, E. M., and Derisio, C. Environmental and biological  
843 factors controlling the spring phytoplankton bloom at the Patagonian shelf break front—Degraded fucoxanthin pigments and  
844 the importance of microzooplankton grazing. *Prog. Oceanogr.*, 146, 1-21, <https://doi.org/10.1016/j.pocean.2016.05.002>,  
845 2016.

846 Combes, V. and Matano, R. P. The Patagonian shelf circulation: Drivers and variability. *Prog Oceanogr.* 167: 24-43,  
847 <https://doi.org/10.1016/j.pocean.2018.07.003>, 2018.



- 848 D'Agostino, V.C., Krock, B., Degradi, M., Sastre, V., Santinelli, N., Krohn, T. and Hoffmeyer, M. S. Occurrence of toxigenic  
849 microalgal species and phycotoxin accumulation in mesozooplankton in northern Patagonian gulfs, Argentina. *Environ.*  
850 *Toxicol. Chem.* 38(10), 2209-2223, <https://doi.org/10.1002/etc.4538>, 2019.
- 851 Delgado, A. L., Hernández-Carrasco, I., Combes, V., Font-Muñoz, J., Pratolongo, P. D., and Basterretxea, G. Patterns and  
852 trends in chlorophyll-*a* concentration and phytoplankton phenology in the biogeographical regions of Southwestern Atlantic.  
853 *J. Geophys. Res.: Oceans*, 128(9), e2023JC019865, <https://doi.org/10.1029/2023JC019865>, 2023.
- 854 Della Penna, A., De Monte, S., Kestenare, E., Guinet, C., and d'Ovidio, F. Quasi-planktonic behavior of foraging top marine  
855 predators. *Scientific Reports*, 5(1), 18063, <https://doi.org/10.1038/srep18063>, 2015.
- 856 d'Ovidio, F., Fernández, V., Hernández-García, E. and López, C. Mixing structures in the mediterranean sea from finite-size  
857 Lyapunov exponents. *Geophys. Res. Lett.* 31, 17203, <https://doi.org/10.1029/2004GL020328>, 2004.
- 858 d'Ovidio, F., Isern-Fontanet, J., López, C., Hernández-García, E. and García-Ladona, E. Comparison between Eulerian  
859 diagnostics and finite-size Lyapunov exponents computed from altimetry in the Algerian basin. *Deep-Sea Res. I* 56, 15–  
860 31, <https://doi.org/10.1016/j.dsr.2008.07.014>, 2009.
- 861 Fabro, E., Almandoz, G. O., Krock, B., and Tillmann, U. Field observations of the dinoflagellate genus *Azadinium* and  
862 azaspiracid toxins in the south-west Atlantic Ocean. *Mar. Freshw. Res.* 71 (7), 832–843, <https://doi.org/10.1071/MF19124>,  
863 2019.
- 864 Ferronato C., Berden G., Rivarossa M. and Guinder V.A. Wind-driven currents and water masses shape spring phytoplankton  
865 distribution and composition in hydrologically complex, productive shelf waters. *Limnol. Oceanogr.*,  
866 <https://doi.org/10.1002/lno.12413>, 2023.
- 867 Ferronato, C., Guinder, V.A., Rivarossa, M., Saraceno, M., Ibarbalz, F., Tillmann, U., Almandoz, G., Bourdin, G.,  
868 D'Agostino, V., Gilibert, A., Loizaga, R., López Abbate, C., Nocera, A. C., Silva, R., and Flombaum, P. Insights into  
869 protistan plankton blooms in the stirred Southwestern Atlantic Ocean. *J. Geophys. Res.: Oceans*. Under revision, MS ID:  
870 2024JC021412, 2024.
- 871 Frey, D. I., Piola, A. R., and Morozov, E. G. Convergence of the Malvinas current branches near 44° S. *Deep Sea Research*  
872 *Part I: Oceanogr. Res. Papers*, 104023, <https://doi.org/10.1016/j.dsr.2023.104023>, 2023.
- 873 García, V. M. T., Garcia, C. A. E., Mata, M. M., Pollery, R. C., Piola, A. R., Signorini, S. R., McClain, C. R., and Iglesias-  
874 Rodríguez, M. D. Environmental factors controlling the phytoplankton blooms at the Patagonia shelf break in spring. *Deep-*  
875 *Sea Res. I: Oceanogr. Res. Pap.* 55(9): 1150-1166, <https://doi.org/10.1016/j.dsr.2008.04.011>, 2008.
- 876 GEBCO Compilation Group, General Bathymetric Chart of the Ocean. GEBCO 2021 grid.  
877 [https://www.gebco.net/data\\_and\\_products/historical\\_data\\_sets/#gebco\\_2021](https://www.gebco.net/data_and_products/historical_data_sets/#gebco_2021), 2021.
- 878 Genitsaris, S., Stefanidou, N., Sommer, U. and Moustaka-Gouni, M. Phytoplankton blooms, red tides and mucilaginous  
879 aggregates in the urban Thessaloniki Bay, Eastern Mediterranean. *Diversity*, 11(8), 136, <https://doi.org/10.3390/d11080136>,  
880 2019.
- 881 Giddings, S. N., MacCready, P., Hickey, B. M., Banas, N. S., Davis, K. A., Siedlecki, S. A., Trainer, V. L., Kudela, R. M.,  
882 Pelland, N. A., and Connolly, T. P. Hindcasts of potential harmful algal bloom transport pathways on the Pacific Northwest  
883 coast. *J. Geophys. Res.: Oceans* 119 (4), 2439–2461, <https://doi.org/10.1002/2013JC009622>, 2014.
- 884 Glibert, P. M. Margalef revisited: a new phytoplankton mandala incorporating twelve dimensions, including nutritional  
885 physiology. *Harmful Algae*, 55, 25-30, <https://doi.org/10.1016/j.hal.2016.01.008>, 2016.
- 886 Guinder, V.A., Ferronato, C., Segura, V., Dogliotti, A., and Lutz, V. The phytoplankton of the Patagonian shelf break *Front.*  
887 *In: The Patagonian shelf-break Front. Ecology, Fisheries, Wildlife Conservation*. Acha, M., Iribarne, O., Piola, A. (Eds).  
888 Springer Nature. ISBN: 978-3-031-71189-3, 2024.
- 889 Guinder V.A., Tillmann U., Krock B., Delgado A., Garzón Cardona J.E., Katja M., López Abbate M.C., Silva R. and Lara  
890 R. Plankton multiproxy analyses in the Northern Patagonian Shelf, Argentina: community structure, phycotoxins and



- 891 characterization of toxic *Alexandrium* strains. *Front. Mar. Sci.* 5: 394, <https://doi.org/10.3389/fmars.2018.00394>, 2018.
- 892 Guinder, V. A., Malits, A., Ferronato, C., Krock, B., Garzón-Cardona, J. E., and Martínez, A. Microbial plankton  
893 configuration in the epipelagic realm from the Beagle Channel to the Burdwood Bank, a Marine Protected Area in Sub-  
894 Antarctic waters. *Plos One* 15(5): e0233156, <https://doi.org/10.1371/journal.pone.0233156>, 2020.
- 895 Hallegraeff, G. M., Anderson, D. M., Belin, C., Bottein, M. Y. D., Bresnan, E., Chinain, M., Enevoldsen, H., Iwataki, M.,  
896 Karlson, B., McKenzie, C.H., Sunesen, I., Pitcher, G. C., Provoost, P., Richardson, A., Schweibold, L., Tester, P. A., Trainer,  
897 V. L., Yniguez, A. T., and Zingone, A. Perceived global increase in algal blooms is attributable to intensified monitoring and  
898 emerging bloom impacts. *Commun. Earth Environ.* 2 (1), 1–10, <https://doi.org/10.1038/s43247-021-00178-8>, 2021.
- 899 Haller, G. and Beron-Vera, F. J. Geodesic theory of transport barriers in two-dimensional flows. *Phys. D: Nonlinear Phenom.*,  
900 241(20), 1680-1702, <https://doi.org/10.1016/j.physd.2012.06.012>, 2012.
- 901 Hansen, H. P., Koroleff, F. Determination of nutrients. *Methods of seawater analysis*, (Grasshoff, K., Kremling, K. and  
902 Ehrhardt, M. (Eds.). Verlag Chemie, 159-228, 1999.
- 903 Hasle, G., 1987. Concentrating phytoplankton. Settling. The inverted microscope method. In: Sournia, A. (Ed.). *Monographs*  
904 *on Oceanographic Methodology: Phytoplankton Manual*. Unesco, Paris, pp. 88–96.
- 905 Hernández-Carrasco I., Alou-Font E., Dumont P. A., Cabornero A., Allen J., and Orfila A. Lagrangian flow effects on  
906 phytoplankton abundance and composition along filament-like structures. *Prog. Oceanogr.*, 189, 102469,  
907 <https://doi.org/10.1016/j.pocean.2020.102469>, 2020.
- 908 Jeffrey S. T. and Humphrey G. F. New spectrophotometric equations for determining chlorophylls *a*, *b*, *c*<sub>1</sub> and *c*<sub>2</sub> in higher  
909 plants, algae and natural phytoplankton. *Biochem. Physiol. Pflanzen*, 167(2), 191-194, [https://doi.org/10.1016/S0015-](https://doi.org/10.1016/S0015-3796(17)30778-3)  
910 [3796\(17\)30778-3](https://doi.org/10.1016/S0015-3796(17)30778-3), 1975.
- 911 Kelley, D. E., Richards, C. and Layton, C. oce: An R package for oceanographic analysis. *J. Open Source Softw.* 7: 3594,  
912 2022.
- 913 Krock, B., Tillmann, U., Tebben, J., Trefault, N., and Gu, H. Two novel azaspiracids from *Azadinium poporum*, and a  
914 comprehensive compilation of azaspiracids produced by Amphidomataceae, (Dinophyceae). *Harmful Algae* 82, 1–8,  
915 <https://doi.org/10.1016/j.hal.2018.12.005>, 2019.
- 916 Kuwata, K., Lum, W.M., Takahashi, K., Benico, G., Takahashi, K., Lim, P.T., Leaw, C.P., Uchida, H., Ozawa, M.,  
917 Matsushima, R., Watanabe, R., Suzuki, T., and Iwataki, M. Phylogeny and ultrastructure of a non-toxicogenic dinoflagellate  
918 *Amphidoma fulgens* sp. nov. (Amphidomataceae, Dinophyceae), with a wide distribution across Asian Pacific. *Harmful Algae*  
919 138, 102701, <https://doi.org/10.1016/j.hal.2024.102701>, 2024.
- 920 Lago, L. S., Saraceno, M., Piola, A. R., and Ruiz-Etcheverry, L. A. Volume transport variability on the northern argentine  
921 continental shelf from in situ and satellite altimetry data. *J. Geophys. Res.: Oceans*, 126(2), e2020JC016813,  
922 <https://doi.org/10.1029/2020JC016813>, 2021.
- 923 Lehahn, Y., d'Ovidio, F., Lévy, M., and Heifetz, E. Stirring of the northeast Atlantic spring bloom: A Lagrangian analysis  
924 based on multisatellite data. *J. Geophys. Res.: Oceans*, 112(C8), <https://doi.org/10.1029/2006JC003927>, 2007.
- 925 Lehahn, Y., Koren, I., Sharoni, S., d'Ovidio, F., Vardi, A. and Boss, E. Dispersion/dilution enhances phytoplankton blooms  
926 in low-nutrient waters. *Nat. Commun.*, 8(1), 14868, <https://doi.org/10.1038/ncomms14868>, 2017.
- 927 Lévy, M., Franks, P. J., and Smith, K. S. The role of submesoscale currents in structuring marine ecosystems. *Nat. Commun.*,  
928 9(1), 4758, <https://doi.org/10.1038/s41467-018-07059-3>, 2018.
- 929 Lin S., Litaker R.W. and Sunda, W.G. Phosphorus physiological ecology and molecular mechanisms in marine phytoplankton.  
930 *J. Phycol.*, 52(1), 10-36, <https://doi.org/10.1111/jpy.12365>, 2016.
- 931 Liu M., Tillmann U., Ding G., Wang A. and Gu, H. Metabarcoding revealed a high diversity of Amphidomataceae  
932 (Dinophyceae) and the seasonal distribution of their toxigenic species in the Taiwan Strait. *Harmful Algae*, 124, 102404.  
933 <https://doi.org/10.1016/j.hal.2023.102404>, 2023.



- 934 Lopez-Rivera, A., O'callaghan, K., Moriarty, M., O'Driscoll, D., Hamilton, B., Lehane, M., James, K.J., Furey, A.. First  
935 evidence of azaspiracids (AZAs): a family of lipophilic polyether marine toxins in scallops (*Argopecten purpuratus*) and  
936 mussels (*Mytilus chilensis*) collected in two regions of Chile. *Toxicon* 55 (4), 692–701,  
937 <https://doi.org/10.1016/j.toxicon.2009.10.020>, 2010.
- 938 Mahadevan, A. The impact of submesoscale physics on primary productivity of plankton. *Annu. Rev. Mar. Sci.*, 8(1), 161-  
939 184, <https://doi.org/10.1146/annurev-marine-010814-015912>, 2016.
- 940 Mangolte, I., Lévy, M., Haëck, C., and Ohman, M. D. Sub-frontal niches of plankton communities driven by transport and  
941 trophic interactions at ocean fronts. *Biogeosciences*, 20(15), 3273-3299, <https://doi.org/10.5194/bg-20-3273-2023>, 2023.
- 942 Maritorena, S., d'Andon, O. H. F., Mangin, A., and Siegel, D. A. Merged satellite ocean color data products using a bio-  
943 optical model: Characteristics, benefits and issues. *Remote Sens. Environ.*, 114(8), 1791-1804,  
944 <https://doi.org/10.1016/j.rse.2010.04.002>, 2010.
- 945 Martinetto, P., Alemany, D., Botto, F., Mastrángelo, M., Falabella, Acha, E.M., Antón, G., Bianchi, A., Campagna, C.,  
946 Cañete, G., Filippo, P., Iribarne, O., Laterra, P., Martínez, P., Negri, R., Piola, A.R., Romero, S.I., Santos, D., and Saraceno,  
947 M. Linking the scientific knowledge on marine frontal systems with ecosystem services. *Ambio* 49 (2), 541–556,  
948 <https://doi.org/10.1007/s13280-019-01222-w>, 2019.
- 949 Matano, R. P., Palma, E. D., and Piola, A. R. The influence of the Brazil and Malvinas Currents on the Southwestern Atlantic  
950 Shelf circulation. *Ocean Sci.* 6(4): 983-995, <https://doi.org/10.5194/os-6-983-2010>, 2010.
- 951 McGirr, S., Clarke, D., Kilcoyne, Silke, J., and Touzet, N. Co-localisation of Azaspiracid Analogs with the Dinoflagellate  
952 Species *Azadinium spinosum* and *Amphidoma languida* in the Southwest of Ireland. *Microb Ecol* 83, 635–646,  
953 <https://doi.org/10.1007/s00248-021-01777-w>, 2022.
- 954 Palma, E. D., Matano, R. P., and Piola, A. R. A numerical study of the southwestern Atlantic shelf circulation: Stratified Ocean  
955 response to local and offshore forcing. *J. Geophys. Res.* <https://doi.org/10.1029/2007jc004720>, 2008.
- 956 Piola, A. R., Bodnariuk, N., Combes, V., Franco, B. C., Matano, R. P., Palma, E. D., Romero, S. I., Saraceno, M., Urricariet,  
957 M. M. Anatomy and dynamics of the Patagonia shelf break front. In: *The Patagonian shelf-break Front. Ecology, Fisheries,*  
958 *Wildlife Conservation.* Acha, M., Iribarne, O., Piola, A. (Eds). Springer Nature. ISBN: 978-3-031-71189-3, 2024.
- 959 Ramírez F.J., Guinder V.A., Ferronato C. and Krock B. Increase in records of toxic phytoplankton and associated toxins in  
960 water samples in the Patagonian Shelf (Argentina) over 40 years of field surveys. *Harmful Algae*, 118: 102317,  
961 <https://doi.org/10.1016/j.hal.2022.102317>, 2022.
- 962 Raine, R. A review of the biophysical interactions relevant to the promotion of HABs in stratified systems: the case study of  
963 Ireland. *Deep Sea Res. Part II* 101, 21–31, <https://doi.org/10.1016/j.dsr2.2013.06.021>, 2014.
- 964 Rossi, R., Dell'Aversano, C., Krock, B., Ciminiello, P., Percopo, I., Tillmann, U., Soprano, V., and Zingone, A. Mediterranean  
965 *Azadinium dexteroporum* (Dinophyceae) produces AZA-35 and six novel azaspiracids: a structural study by a multi-platform  
966 mass spectrometry approach. *Anal. Bioanal. Chem.* 409, 1121-1134, <https://doi.org/10.1007/s00216-016-0037-4>, 2017.
- 967 Salas R., Tillmann U., Gu H., Wietkamp S., Krock B. and Clarke D. Morphological and molecular characterization of multiple  
968 new *Azadinium* strains revealed a high diversity of non-toxigenic species of Amphidomataceae (Dinophyceae) including two  
969 new *Azadinium* species in Irish waters, North East Atlantic. *Phycol. Res.*, 69(2), 88-115, <https://doi.org/10.1111/pre.12448>,  
970 2021.
- 971 Salyuk P.A., Mosharov S.A., Frey D.I., Kasyan V.V., Ponomarev V.I., Kalinina O.Y., Morozov E.G., Latushkin A.A.,  
972 Sapozhnikov P.V., Ostroumova S.A., Lipinskaya N.A., Budyansky M.V., Chukmasov P.V., Krechik V.A., Uleysky M.Y.,  
973 Fayman P.A., Mayor A.Y., Mosharova I.V., Chernetsky A.D., Shkorba S.P. and Shved N. A. Physical and biological features  
974 of the waters in the outer Patagonian shelf and the Malvinas Current. *Water*, 14(23), 3879, <https://doi.org/10.3390/w14233879>,  
975 2022.





- 976 Ser-Giacomi, E., Martínez-García, R., Dutkiewicz, S., and Follows, M. J. A. Lagrangian model for drifting ecosystems reveals  
977 heterogeneity-driven enhancement of marine plankton blooms. *Nat. Commun.* 14(1), 6092, [https://doi.org/10.1038/s41467-](https://doi.org/10.1038/s41467-023-41469-2)  
978 [023-41469-2](https://doi.org/10.1038/s41467-023-41469-2), 2023.
- 979 Smayda, T.J. Turbulence, watermass stratification and harmful algal blooms: an alternative view and frontal zones as “pelagic  
980 seed banks”. *Harmful Algae* 1 (1), 95–112, [https://doi.org/10.1016/S1568-9883\(02\)00010-0](https://doi.org/10.1016/S1568-9883(02)00010-0), 2002.
- 981 Sunesen, I., Méndez, S. M., Mancera-Pineda, J. E., Dechraoui-Bottein, M. Y., and Enevoldsen, H. The Latin America and  
982 Caribbean HAB status report based on OBIS and HAEDAT maps and databases. *Harmful Algae* 102, 101920,  
983 <https://doi.org/10.1016/j.hal.2020.101920>, 2021.
- 984 Tillmann, U., Salas, R., Gottschling, M., Krock, B., O’Driscoll, D., and Elbrächter, M. *Amphidoma languida* sp. nov.  
985 (Dinophyceae) reveals a close relationship between *Amphidoma* and *Azadinium*. *Protist* 163, 701-719,  
986 <https://doi.org/10.1016/j.protis.2011.10.005>, 2012.
- 987 Tillmann, U., and Akselman, R. Revisiting the 1991 algal bloom in shelf waters off Argentina: *Azadinium luciferelloides* sp.  
988 nov. (Amphidomataceae, Dinophyceae) as the causative species in a diverse community of other amphidomataceans. *Phycol.*  
989 *Res.* 64, 160-175, <https://doi.org/10.1111/pre.12133>, 2016.
- 990 Tillmann, U., Trefault, N., Krock, B., Parada-Pozo, G., De la Iglesia, R., and Vásquez, M. Identification of *Azadinium poporum*  
991 (Dinophyceae) in the Southeast Pacific: morphology, molecular phylogeny, and azaspiracid profile characterization. *J. Plank.*  
992 *Res.* 39 (2), 350–367, <https://doi.org/10.1093/plankt/fbw099>, 2017a.
- 993 Tillmann, U., Sánchez-Ramírez, S., Krock, B., and Bernales-Jiménez, A. A bloom of *Azadinium polongum* in coastal waters  
994 off Peru. *Rev. Biol. Mar. Oceanogr.* 52(3), 591-610, <http://dx.doi.org/10.4067/S0718-19572017000300015>, 2017b.
- 995 Tillmann, U. Amphidomataceae. In: Shumway, S.E., Burkholder, J.M., Morton, S. L. (Eds.), *Harmful Algal Blooms: A*  
996 *compendium Desk Reference*. Wiley, Singapore, pp. 575–582, ISBN: 978-1-118-99467-2, 2018.
- 997 Tillmann, U. Electron microscopy of a 1991 spring plankton sample from the Argentinean shelf reveals the presence of four  
998 new species of Amphidomataceae (Dinophyceae). *Phycol. Res.* 66, 269-290, <https://doi.org/10.1111/pre.12225>, 2018.
- 999 Tillmann, U., Gottschling, M., Guinder, V. and Krock, B. *Amphidoma parvula* (Amphidomataceae), a new planktonic  
1000 dinophyte from the Argentine Sea. *Eur. J. Phycol.* 53, 14-28, <https://doi.org/10.1080/09670262.2017.1346205>, 2018.
- 1001 Tillmann, U., Gottschling, M., Krock, B., Smith, K.F. and Guinder, V.A. High abundance of Amphidomataceae  
1002 (Dinophyceae) during the 2015 spring bloom of the Argentinean Shelf and a new, non-toxicogenic ribotype of *Azadinium*  
1003 *spinosum*. *Harmful Algae*, 84: 244-260, <https://doi.org/10.1016/j.hal.2019.01.008>, 2019.
- 1004 Tillmann, U., Wietkamp, S., Krock, B., Tillmann, A., Voss, D. and Gu, H. Amphidomataceae (Dinophyceae) in the western  
1005 Greenland area, including the description of *Azadinium perforatum* sp. nov. *Phycologia* 59, 63-88,  
1006 <https://doi.org/10.1080/00318884.2019.1670013>, 2020.
- 1007 Tillmann, U., Wietkamp, S., Gu, H., Krock, B., Salas, R. and Clarke, D. Multiple new strains of Amphidomataceae  
1008 (Dinophyceae) from the North Atlantic revealed a high toxin profile variability of *Azadinium spinosum* and a new non-  
1009 toxicogenic *Az. cf. spinosum*. *Microorganisms*, 9(1), 134, <https://doi.org/10.3390/microorganisms9010134>, 2021.
- 1010 Turner, A.D. and Goya, A.B. Occurrence and profiles of lipophilic toxins in shellfish harvested from Argentina. *Toxicon* 102,  
1011 32–42, <https://doi.org/10.1016/j.toxicon.2015.05.010>, 2015.
- 1012 Wietkamp, S., Krock, B., Clarke, D., Voß, D., Salas, R., Kilcoyne, J., and Tillmann, U. Distribution and abundance of  
1013 azaspiracid-producing dinophyte species and their toxins in North Atlantic and North Sea waters in summer 2018. *PLoS One*  
1014 15, e0235015, <https://doi.org/10.1371/journal.pone.0235015>, 2020.
- 1015 Wilson, C., Sastre, A. V., Hoffmeyer, M., Rowntree, V. J., Fire, S. E., Santinelli, N. H., Ovejero, S. D., D’Agostino, V., Marón,  
1016 C. F., Doucette, G. J., Broadwater, M. H., Wang, Z., Montoya, N., Seger, J., Adler, F. R., Sironi, M. and Uhart M. M., Southern  
1017 right whale (*Eubalaena australis*) calf mortality at Península Valdés, Argentina: Are harmful algal blooms to blame? *Mar.*  
1018 *Mammal Sci.* 32(2): 423-451, <https://doi.org/10.1111/mms.12263>, 2015.